A&A 491, 89–111 (2008)
DOI: 10.1051/0004-6361:200809648

Astronomy & Astrophysics

3D Lyα radiation transfer

III. Constraints on gas and stellar properties of $z \sim 3$ Lyman break galaxies (LBG) and implications for high-z LBGs and Lyα emitters

A. Verhamme[1], D. Schaerer[1,2], H. Atek[3], and C. Tapken[4]

[1] Geneva Observatory, University of Geneva, 51 Ch. des Maillettes, 1290 Versoix, Switzerland
e-mail: anne.verhamme@unige.ch
[2] Laboratoire d'Astrophysique de Toulouse-Tarbes, Université de Toulouse, CNRS, 14 Avenue E. Belin, 31400 Toulouse, France
[3] Institut d'Astrophysique de Paris, 98bis boulevard Arago, 75014 Paris, France
[4] Max Planck Institute for Astronomy, Königstuhl 17, 69117 Heidelberg, Germany

Received 25 February 2008 / Accepted 22 May 2008

ABSTRACT

Aims. The aim of our study is to understand the variety of observed Lyα line profiles and strengths in Lyman Break Galaxies (LBGs) and Lyα emitters (LAEs), the physical parameters governing them, and hence derive constraints on the gas and dust content and stellar populations of these objects.

Methods. Using our 3D Lyα radiation transfer code including gas and dust, MCLya, we fit 11 LBGs from the FORS Deep Field with redshifts between 2.8 and 5. A simple geometry of a spherically expanding shell of H I is adopted.

Results. The variety of observed Lyα profiles is successfully reproduced. Most objects show outflow velocities of $V_{\rm exp} \sim 150-200$ km s^{-1}; two objects are most likely quasi-static. The radial H I column density ranges from $N_{\rm HI} \sim 2\times10^{19}$ to 7×10^{20} cm^{-2}. Our Lyα profile fits yield values of $E(B-V) \sim 0.05-0.2$ for the gas extinction. We find indications for a dust-to-gas ratio higher than the Galactic value, and for a substantial scatter. The escape fraction of Lyα photons is found to be determined primarily by the extinction, and a simple fit formula is proposed. In this case a measurement of $EW({\rm Ly}\alpha)_{\rm obs}$ can yield $E(B-V)$, if the intrinsic Lyα equivalent width is known (or assumed). Intrinsic $EW({\rm Ly}\alpha)_{\rm int} \sim 50-100$ Å are found for 8/11 objects, as expected for stellar populations forming constantly over long periods ($\gtrsim$10−100 Myr). In three cases we found indications of younger populations. Our model results also allow us to understand observed correlations between $EW({\rm Ly}\alpha)_{\rm obs}$ and other observables such as $FWHM({\rm Ly}\alpha)$, $E(B-V)$, SFR(UV) etc.

We suggest that most observed trends of Lyα, both in LBGs and LAEs, are driven by variations of $N_{\rm HI}$ and the accompanying variation of the dust content. Ultimately, the main parameter responsible for these variations may be the galaxy mass. We also show that there is a clear overlap between LBGs and LAEs: at $z \sim 3$ approximately 20−25% of the LBGs of Shapley et al. (2003, ApJ, 588, 65) overlap with ∼23% of the LAEs of Gronwal et al. (2007, ApJ, 667, 79). Radiation transfer and dust effects explain the increase of the LAE/LBG ratio, and a higher percentage of LBGs with strong Lyα emission with increasing redshift.

Key words. line: profiles – radiative transfer – galaxies: starburst – galaxies: ISM – galaxies: high-redshift – ultraviolet: galaxies

1. Introduction

Lyα line radiation, often of the brightest emission lines in distant star-forming galaxies, is now frequently observed over a wide redshift range (e.g. Hu et al. 1998; Kudritzki et al. 2000; Malhotra & Rhoads 2002; Ajiki et al. 2003; Taniguchi et al. 2005; Shimasaku et al. 2006; Kashikawa et al. 2006; Tapken et al. 2006; Gronwall et al. 2007; Ouchi et al. 2007). Numerous narrow-band and other surveys use this line to search for galaxies at specific cosmic ages, and to hunt for the most distant objects in the universe (see Willis & Courbin 2005; Cuby et al. 2007; Stark et al. 2007a). Extremely deep "blind" spectroscopic exposures have revealed very faint objects through their Lyα emission (Rauch et al. 2007), illustrating the discovery potential of future instruments such as the Multi Unit Spectroscopic Explorer (MUSE) for the Very Large Telescope (VLT) and extremely large telescopes.

Lyα measurements are used to infer a number of properties such as redshift, star formation rates, constraints on the ionisation of the intergalactic medium and hence on cosmic reionisation, trace large scale structure at high redshift etc. (see e.g. Schaerer 2007, for an overview, and references therein). However, given the physics of this generally optically thick resonance line, quantitative interpretations of Lyα are often difficult or even ambiguous, as shown by detailed studies of nearby starbursts carried out during the last decade (Lequeux et al. 1995; Kunth et al. 1998; Mas-Hesse et al. 2003; Hayes et al. 2005, 2007; Atek et al. 2008).

With the increased computer power and the availability of Lyα radiation transfer codes (cf. Ahn et al. 2000, 2002; Cantalupo et al. 2005; Hansen & Oh 2006; Dijkstra et al. 2006a; Tasitsiomi 2006; Verhamme et al. 2006; Pierleoni et al. 2007; Laursen et al. 2008) we can not only predict Lyα in different astrophysical situations (e.g. galaxy and cosmological simulations) but also compare observed Lyα properties (line profiles, equivalent widths, etc.) of individual galaxies (nearby and distant ones) with detailed 3D radiation transfer calculations. This is one of the aims of our paper.

Two galaxy populations, the well known Lyman Break Galaxies (LBGs) and the Lyα emitters (LAEs), currently represent the largest samples of distant galaxies, at least from $z \sim 3$ to 6.5. Important questions remain unanswered about them, closely related to their Lyα emission and absorption.

LBGs show a great diversity of Lyα profiles and strengths, reaching from strong emission, over P-Cygni type profiles, to strong absorption (see e.g. Shapley et al. 2003). Furthermore the Lyα properties are found to correlate with other quantities such as the strength of interstellar lines (IS), extinction, the star formation rate (SFR) etc. However, the origin of these variations and correlations remains largely unknown or contradictory at best. For example, Shapley et al. (2001) suggested age as the main difference between LBG groups with different Lyα strength, where objects with Lyα in absorption would be younger and more dusty. However, it is not clear why older LBGs would contain less dust, especially since outflows, supposedly used to expel the dust, are ubiquitous in all LBGs and since these outflows are the location where the emergent Lyα spectrum is determined. Ferrara & Ricotti (2006) proposed that LBGs host short-lived (30 ± 5 Myr) starburst episodes, whose outflows – when observed at different evolutionary phases – would give rise to the observed correlations between IS lines and Lyα. However, the ages obtained from SED and spectral fits of LBGs show older ages and fairly constant star formation histories (cf. Ellingson et al. 1996; Pettini et al. 2000; Shapley et al. 2001; Papovich et al. 2001; Pentericci et al. 2007). Pentericci et al. (2007) find that $z \sim 4$ LBGs without Lyα emission are on average somewhat older ($\sim 410 \pm 70$ versus 200 ± 50 Myr) and more massive than those with Lyα in emission. However, given the significant amount of ongoing star formation inferred for both galaxy subsample types (with/without Lyα emission) from their SED fits, intrinsic Lyα emission is expected in both subsamples. The apparent differences in age and ratio of age over star formation time scale (τ) can therefore not be a physical cause of the observed Lyα variations. Erb et al. (2006), from an analysis of $z \sim 2$ LBGs, also find that more massive galaxies have fainter Lyα (or Lyα in absorption); following the arguments of Mas-Hesse et al. (2003) they suggest that this is mostly due to an increased velocity dispersion of the interstellar medium, indicated by the increased strength of the saturated IS lines, which would increase the fraction of Lyα being absorbed. However, from radiation transfer modelling we find that the behaviour of the Lyα escape fraction is not linear with the velocity dispersion in the ISM (Verhamme et al. 2006, and below). Other physical parameters may play a more important role in the destruction of Lyα.

Important questions also remain concerning the properties of LAEs, their similarities and differences with respect to LBGs, and about the overlap between these galaxy populations. Since a fraction of LBGs show strong enough Lyα emission to be detected with the narrow-band technique mostly used to find LAEs there must definitely be an overlap. For example, at $z \sim 3$ approximately 25% of the LBGs of Steidel and collaborators (Shapley et al. 2003) have $EW(\mathrm{Ly}\alpha)_{\mathrm{obs}} \gtrsim 20$ Å (restframe), sufficient to be detected in the LAE survey of Gronwall et al. (2007). However, what the properties of LAEs are e.g. in terms of stellar populations (age, star formation histories, ...), mass, dust content, outflows, metallicity etc. is not yet well established, although the first such analyses have recently become available (see Schaerer & Pelló 2005; Lai et al. 2007, 2008; Gronwall et al. 2007; Gawiser et al. 2007; Pirzkal et al. 2007; Finkelstein et al. 2007b). Understanding the nature of LAEs and their relation to LBGs is also crucial since the contribution of the LAE population to the known starburst population seems to increase with redshift (Hu et al. 1998; Shimasaku et al. 2006; Nagao et al. 2007; Ouchi et al. 2007; Dow-Hygelund et al. 2007; Reddy et al. 2007).

Several types of theoretical models have been constructed during the last few years aimed at understanding LAE and LBG populations, the relation between the two populations, and to use them as constraints for galaxy formation scenarios, cosmic reionisation, and other topics (Thommes & Meisenheimer 2005; Le Delliou et al. 2006; Mori & Umemura 2006; Dijkstra & Wyithe 2007; Kobayashi et al. 2007; Mao et al. 2007; Stark et al. 2007b; Nagamine et al. 2008). Observational constraints on crucial parameters such as the Lyα escape fraction from LBGs and LAEs, and other insight from radiation transfer models are, however, badly needed to reduce uncertainties and degeneracies in these modeling approaches.

With these questions about LBGs and LAEs in mind, we have recently started to model a variety of $z \sim 3$ starbursts with our new Lyα radiation transfer code (Verhamme et al. 2006, Paper I). First we studied the well known $z \sim 2.7$ LBG MS1512-cB58 (cB58 for short), whose spectrum is dominated by strong Lyα absorption (Schaerer & Verhamme 2008, Paper II). In this third paper of the series we present an analysis of 11 LBGs observed with FORS2 at the VLT with sufficient spectral resolution ($R \sim 2000$) to allow detailed Lyα profile fitting to constrain their properties. Taken together, the objects analysed in Papers II and III cover a wide range of Lyα strengths and also different morphologies, including absorption dominated Lyα and Lyα emission lines with equivalent widths between ~6 and 150 Å (restframe). The variety of objects modeled in Papers II and III thus covers in particular the entire range of Lyα strengths defining the 4 spectral groups of the LBG sample of Shapley et al. (2003), the largest currently available at $z \sim 3$. Furthermore, several of the objects we model have strong enough Lyα emission to classify as LAEs, according to the criteria used in many surveys. Our analysis represents the first modeling attempt of Lyα line profiles of high redshift galaxies with a detailed radiation transfer code including gas and dust and treating line and continuum radiation.

The remainder of the paper is structured as follows. A description of the radiation transfer code, the assumptions, and input parameters is given in Sect. 2. In Sect. 3 we model the Lyα profiles of the individual objects. Our main fitting results are discussed and compared with other observations in Sect. 4. Other properties are derived in Sect. 5. In Sect. 6 we propose a unifying scenario for LBGs and LAEs and discuss several implications. Our main conclusions are summarised in Sect. 7.

2. Lyα radiation transfer modeling

To fit the observations we used our 3D Monte Carlo (MC) radiation transfer code *MCLya* (Verhamme et al. 2006). The code solves the transfer of the Lyα line and adjacent continuum photons including the detailed processes of Lyα line scattering, dust scattering, and dust absorption. The main assumptions required for the modeling concern the geometry, the choice of the input parameters, and the input spectrum. We discuss them now in turn.

2.1. Geometry

For simplicity, and given empirical evidence in favour of a fairly simple geometry in $z \sim 3$ LBGs discussed by Verhamme et al. (2006), we adopted first a simple "super-bubble" model to

Table 1. Sample of 11 LBG galaxies taken from Tapken et al. (2006) with their observational constraints.

ID	type	z	$SFR_{\rm UV}$ [$M_\odot\,{\rm yr}^{-1}$]	$SFR_{\rm Ly\alpha}$ [$M_\odot\,{\rm yr}^{-1}$]	β	Δv(em − abs) [km s^{-1}]	$EW({\rm Ly}\alpha)_{\rm obs}$ [Å]	$FWHM({\rm Ly}\alpha)_{\rm obs}$ [km s^{-1}]
1267	C	2.788 ± 0.001	1.16 ± 0.25	1.49 ± 0.08			129.8 ± 27.41	235 ± 34
1337	A	3.403 ± 0.004	27.28 ± 1.15	2.10 ± 0.14	−2.43	607	6.69 ± 0.46	597 ± 84
2384	A	3.314 ± 0.004	22.74 ± 0.77	10.8 ± 0.27	−0.55		83.19 ± 3.89	283 ± 47
3389	A	4.583 ± 0.006	14.85 ± 2.47	9.20 ± 0.38			38.82 ± 10.95	354 ± 70
4454	A	3.085 ± 0.004	1.98 ± 0.49	2.25 ± 0.08	−2.42		74.38 ± 11.84	323 ± 47
4691	B	3.304 ± 0.004	17.88 ± 0.75	16.31 ± 0.14	−2.46		79.44 ± 1.61	840 ± 115
5215	C	3.148 ± 0.004	26.20 ± 0.80	9.57 ± 0.21	−1.71		32.48 ± 1.06	483 ± 90
5550	A	3.383 ± 0.004	44.78 ± 1.07	3.27 ± 0.20	−1.81	620	6.36 ± 0.40	424 ± 85
5812	A	4.995 ± 0.006	5.24 ± 0.79	9.60 ± 0.18			153.8 ± 26.6	226 ± 23
6557	A	4.682 ± 0.006	13.85 ± 1.39	3.35 ± 0.15			30.51 ± 3.04	380 ± 135
7539	B	3.287 ± 0.003	29.87 ± 0.78	2.45 ± 0.46	−1.74	80	6.84 ± 0.46	1430 ± 230

ID (Col. 1), Lyα profile type (2), systemic redshift from Noll et al. (2004) except for FDF1267, where z is from T07 (3), the UV (4) and Lyα (5) star formation rate, the slope of the UV continuum β (6), the velocity shift between the LIS lines and Lyα, Δv(em − abs) (7), the observed $EW({\rm Ly}\alpha)_{\rm obs}$ (8) and $FWHM({\rm Ly}\alpha)_{\rm obs}$ (9). *EW*s and *FWHM* are given in the restframe; we here denote them by "observed" for distinction with "intrinsic" or "theoretical" values to be derived later.

attempt to fit the observed Lyα line profile. The assumed geometry is that of an expanding, spherical, homogeneous, and isothermal shell of neutral hydrogen surrounding a central starburst emitting a UV continuum plus Lyα recombination line radiation from its associated H II region. We assume that dust and H I are uniformly mixed.

The homogeneity and a large covering factor of the absorbing medium are supported by observations of LBGs and nearby starbursts. For example, the outflow of cB58 is located well in front of the stars and covers them almost completely, since it absorbs almost all the UV light from the background stars. Indeed, Savaglio et al. (2002) find only a small residual mean flux above the zero level in the core of the Lyα absorption feature, whereas it is black for Pettini et al. (2002). Heckman et al. (2001) estimate an area covering factor for optically thick gas of 98% from the residual intensity at the core of the C II λ1335 line. A somewhat lower covering factor may be indicated for LBGs with strong Lyα emission (Shapley et al. 2003). For simplicity, and in the absence of further observational constraints, we will assume a covering factor of unity.

2.2. Shell parameters

As described in Paper II, the outflow is modelled by a spherical, homogeneous, and isothermal shell of neutral hydrogen and dust centered on a point source. Four parameters characterise the physical conditions in the shell:

- the expansion velocity $V_{\rm exp}$;
- the Doppler parameter b;
- the neutral hydrogen column density $N_{\rm HI}$;
- the dust absorption optical depth $\tau_{\rm a}$.

In principle $V_{\rm exp}$ is constrained by observations, either directly measured by the blueshift of low ionisation interstellar lines (hereafter LIS) compared to stellar lines (Pettini et al. 2002), or from the shift between absorption LIS lines and Lyα in emission, Δv(em − abs), when the stellar lines are too faint to be observed (Shapley et al. 2003). Otherwise $V_{\rm exp}$ will be constrained by Lyα line profile fits. In Verhamme et al. (2006) we showed that radiation transfer effects lead to $\Delta v({\rm em}-{\rm abs}) \approx 3 \times V_{\rm exp}$ in expanding shells with $N_{\rm HI} \gtrsim 10^{20}$ cm^{-2}. For lower column densities the peak of the redshifted Lyα emission may trace $\sim V_{\rm exp}$ (leading to $\Delta v({\rm em}-{\rm abs}) \sim 2V_{\rm exp}$), instead of twice this value (cf. Verhamme et al. 2006, and also Fig. 17). For three of the 11 objects to be modeled here Δv(em − abs) has been measured (see Table 1).

The Doppler parameter b, describing the random motions of the neutral gas possibly including microturbulence, is kept as a free parameter. $b \sim 13$ km s^{-1} corresponds to thermal motion for $T = 10^4$ K; for the lensed LBG cB58 Pettini et al. (2002) derived $b \sim 70$ km s^{-1} from fits of LIS lines.

Although presumably the neutral column density and the dust amount are physically related, e.g. by a given dust-to-gas ratio, both parameters are kept free in our modeling procedure. The resulting values will later be compared to available observational constraints.

We assume that dust and H I are uniformly mixed. As discussed in Verhamme et al. (2006), the dust optical depth $\tau_{\rm a}$ relates to the usual extinction $E(B-V) \approx (0.06 \ldots 0.11)\,\tau_{\rm a}$, where the numerical coefficient covers attenuation/extinction laws of Calzetti et al. (2000), Seaton (1979) and similar. Here we assume $E(B-V) = 0.1\tau_{\rm a}$.

2.3. The intrinsic spectrum in the Lyα region

The synthetic stellar spectrum of star-forming galaxies close to Lyα is described in Paper II. The stellar continuum presents an absorption feature around Lyα whose strength varies in time, depending on the SF history, on the age of the star-forming galaxy, and less on its metallicity (Schaerer 2003; Delgado et al. 2005).

The main H and He recombination lines created in the H II region surrounding the starburst are also predicted by the models of Schaerer (2003, hereafter S03): for metallicities between 1/50 $Z_\odot$ and solar the strength of Lyα varies from $EW({\rm Ly}\alpha)_{\rm int} \sim 250$–$360$ Å at early time after the burst, and declines until zero for a burst whereas it reaches an equilibrium value of 60–100 Å for objects with a constant star formation rate (SFR) after ∼50–100 Myr (see also Fig. 15).

In Paper II, we showed that the fitting of the observed star-forming galaxy cB58 depends only very little on the details of the stellar continuum around Lyα. Since the objects modeled here show stronger Lyα emission than cB58, which is dominated by absorption, neglecting the detailed shape of the stellar continuum is even more justified here. Therefore we model the input

spectrum as a flat continuum plus a Gaussian emission line described by two parameters:

- the equivalent width, $EW(\mathrm{Ly}\alpha)_{\rm int}$; and
- the full width at half maximum, $FWHM(\mathrm{Ly}\alpha)_{\rm int}$.

What "reasonable" values should we adopt for these parameters? Our first approach, to reduce the number of free parameters in the model, was to test if a unique scenario was conceivable, i.e. if we could fit all data with the same intrinsic Lyα spectrum, the differences in the observed spectra would then come from radiation transfer effects in the outflowing medium. These objects are likely starburst galaxies with a constant star formation (SF) history as derived from their UV low/medium-resolution spectra (Noll et al. 2004; Mehlert et al. 2006), so we fix the intrinsic equivalent width to $EW(\mathrm{Ly}\alpha)_{\rm int} = 60{-}100$ Å, as derived from the S03 models. We adopted the intrinsic value $FWHM(\mathrm{Ly}\alpha)_{\rm int} = 100\ \mathrm{km\,s^{-1}}$, as it is comparable to the values measured from the velocity dispersion of Hα and CO lines in cB58(Teplitz et al. 2000; Baker et al. 2004), and the dispersion measured in 16 starbursts at $z \sim 2$ by Erb et al. (2003).

2.4. Description of the method

We ran a grid of ~500 models with varying physical conditions in the shell. The expansion velocity was varied from 0 to 400 $\mathrm{km\,s^{-1}}$ in steps of 50 $\mathrm{km\,s^{-1}}$, the neutral column density from $2{\times}10^{19}$ to $2{\times}10^{21}$ $\mathrm{cm^{-2}}$, the dust amount from $E(B{-}V) = 0$ to 0.4 ($\tau_{\rm a} = 0, 0.1, 0.5, 1., 2., 3.$, and 4.), and the Doppler parameter from $b = 10$ to 200 $\mathrm{km\,s^{-1}}$ (10, 20, 40, 80, and 200 $\mathrm{km\,s^{-1}}$).

In contrast to the four shell parameters, there is no need to run a new Monte Carlo simulation each time we want to change the input Lyα spectrum. This can be made a posteriori without resorting to any simplifying assumption. To do so we run each simulation of the four-dimensional grid with a flat continuum as input spectrum, e.g. the same number of photons per frequency bin, and we record this input frequency for each photon. Once the simulation is done, we construct output spectra corresponding to the input frequency bins and we assign a different weight to each, in order to reconstruct any input spectrum shape (for example, a flat stellar continuum+a Gaussian centered on Lyα, or a synthetic starburst spectrum as in Paper II.

From each calculation we derive the integrated spectrum (Lyα line profile) emerging from the expanding shell. For comparison to the observations, our synthetic spectra are convolved with a Gaussian with $FWHM = 150\ \mathrm{km\,s^{-1}}$ corresponding to the experimental resolution. As shown below, moving in the space of these 6 input parameters, we can reproduce the whole diversity of observed Lyα spectra, ranging from double-peaked profiles to broad absorption or asymmetric emission lines.

Finally, our calculations allow us also to derive the Lyα escape fraction $f_{\rm e}$. This is computed from

$$f_{\rm e} = \frac{\int_{-\infty}^{\infty} f_{\rm e}(v) \times \phi(v)\,\mathrm{d}v}{\int_{-\infty}^{\infty} \phi(v)\,\mathrm{d}v}, \qquad (1)$$

where $\phi(v)$ is the intrinsic Lyα line profile computed from the MC simulation, and $f_{\rm e}(v)$ is the escape fraction in each input frequency bin computed from the MC simulation.

3. Fits of the FORS Deep Field sample

3.1. Description of the FDF sample

Our work uses the FORS Deep Field sample presented by Tapken et al. (2007, hereafter T07). Therefore, we give a brief overview of their work. T07 present the medium-resolution spectra ($R = 2000$) of 16 high-redshift galaxies. The target selection for the objects of T07 was based on the FDF spectroscopic survey (Noll et al. 2004). The FDF spectroscopic survey aimed at obtaining low-resolution spectra ($R \approx 200$) of intrinsically bright galaxies with a photometric redshift (Bender et al. 2001; Gabasch et al. 2004) between $z \approx 1$ and 5 with a high signal-to-noise ratio (≥10). The spectra of 90 galaxies with redshift between 2 and 5 were analysed and published electronically by Noll et al. (2004). The deep (up to 10 h integration time with FORS1/FORS2) low-resolution spectra allowed them to derive the redshift with high accuracy and reliability, and to search for even weak signs of AGN activity of the objects. Based on the low-resolution spectra, T07 selected starburst galaxies with strong Lyα emission and/or with bright UV-restframe continuum for the follow-up medium-resolution spectroscopy.

These medium-resolution spectra were obtained with FORS2 at the VLT UT4 using the holographic grisms 1400 V and 1200 R. The spectral resolution of both grisms is $R \approx 2000$. The spectral range of the 1400 V (1200 R) grism is about 4500 to 5800 (5700 to 7300) Å. All data were collected in service mode using one MXU mask for each grism. The total integration time of the 1400 V (1200 R) observations is 6.25 h (9.45 h). The data were reduced using the MIDAS-based FORS pipeline (Noll et al. 2004). For more details see T07.

The spectra of all objects of T07 include the Lyα profile. However, only eleven Lyα profiles have a sufficient SNR (>10), which allows a detailed comparison with our theoretical models. The properties of this sample are listed in Table 1. Note that except when stated otherwise all equivalent widths are given in the restframe; we denote them by "observed" equivalent widths to distinguish them from "intrinsic" or "theoretical" values to be derived later.

Eight galaxies have redshifts around $z \approx 3$, while 3 galaxies have redshift with $4.5 < z < 5$. While only a few Lyα profiles of our sample show an absorption component (FDF5550), all our profiles display an emission component. The equivalent width of the emission component ranges between $EW(\mathrm{Ly}\alpha)_{\rm obs} = 6$ and 150 Å. This Lyα equivalent width is measured using the continuum redwards of the Lyα emission line (at ≈1300 Å). Although the majority of LBGs have Lyα equivalent widths lower than 20 Å, 8/11 of our galaxies have an equivalent width (of the total Lyα line, including absorption and emission) higher than 20 Å. Therefore 70% of our sample would be detected in a typical narrow-band survey, searching for LAEs.

As described by T07 the profiles show a wide range of morphologies. For convenience, we divide the galaxies in three groups according to their Lyα profile: (A) Lyα emitters with asymmetric profiles: FDF1337, FDF2384, FDF3389, FDF4454, FDF5550, FDF5812, and FDF6557; (B) double-peak profiles FDF4691 and FDF7539; and (C) asymmetric Lyα plus a blue bump: FDF5215 and FDF1267.

3.2. The fitting procedure

For fits with our synthetic spectra the observed, non-normalised spectra were transformed to velocity space using the redshift listed in Table 1. If necessary z was adjusted within the error bars cited. We then use the same normalisation as Tapken et al. (2007) to determine $EW(\mathrm{Ly}\alpha)_{\rm int}$. Finally, we overlay synthetic spectra on observed ones and estimate fit qualities. The spectral parts we focus on are location of the peak, the shape of the peak

Table 2. Summary of the best fits derived from our model of a spherical expanding shell surrounding a starburst to reproduce a sample of 11 spectra from Tapken et al. (2006).

ID	type	$V_{\rm exp}$[km s^{-1}]	b [km s^{-1}]	$N_{\rm HI}$[cm^{-2}]	$\tau_{\rm a}$	EW(Lyα)$_{\rm int}$ [Å]	$FWHM$(Lyα) [km s^{-1}]	$f_{\rm e}$
1337	A	200	20	5×10^{20}	1.0	55	100	0.12
5550	A	200	20	5×10^{20}	1.5	65	100	0.05
2384	A	150	20	3×10^{19}	1.0	170	100	0.16
4454	A	150	20	2×10^{19}	0.5	100	150	0.42
5812	A	150	20	2×10^{19}	1.0	280	100	0.16
3389	A	150	20	2×10^{19}	0.5	50	150	0.45
6557	A	150	20	4×10^{19}	1.0	70	100	0.17
4691	B	10.	20.	8×10^{19}	0.0	80	1000	1.0
7539	B	25.	40.	5×10^{20}	0.5	100	100	0.28
5215	C	200	20	2×10^{15}	0.01	25	700	1.0
5215	C	400	20	7×10^{20}	1.0	120	100	0.12
1267	C	50	20	2×10^{19}	0.1	150	300	0.64
1267	C	300	20	3×10^{20}	2.0	500	100	0.02

Columns 1 and 2 are the object ID and Lyα profile type respectively. Columns 3 to 8 give the model parameters, Col. 9 the derived Lyα escape fraction.

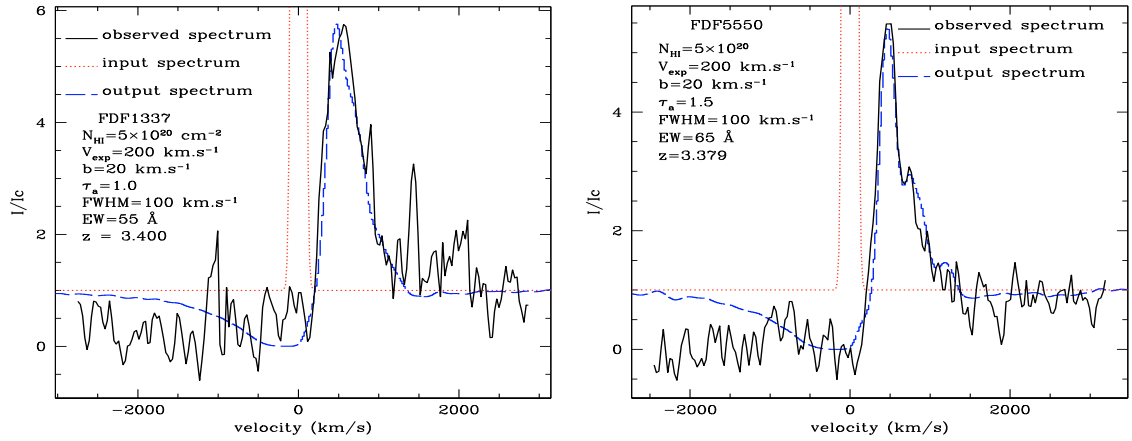

Fig. 1. Lyα line profile fits for FDF1337 (*left*), and FDF550 (*right*), two of the best constrained cases. The observed spectra are shown with the black solid line, model fits as blue dashed curve, the intrinsic (input) profile with the red dotted line. All spectra are normalised to unity in the red (positive velocities). The fit parameters are indicated in the figure and in Table 1. The expanding shell model reproduces well the faint and broad asymmetric Lyα emission lines. The secondary peak, or the "bump" in the red extended wing is also reproduced for $b = 20$ km s^{-1}. Note that the intrinsic EW(Lyα)$_{\rm int}$ of these objects is larger than the observed one by approximately one order of magnitude.

and the extended wing, knowing that the blue side of the spectrum could be affected by the surrounding IGM.

The parameters of the best fits, as well as derived parameters from our model like the escape fraction are summarised in Table 2. Multiple entries correspond to multiple solutions of similar quality.

3.3. The asymmetric profiles (group A)

Among the 11 objects, 7 present the characteristic Lyα asymmetric emission line (FDF1337, 5550, 2384, 4454, 5812, 3389 and 6557). This line shape can be understood by radiation transfer effects through an expanding medium (Verhamme et al. 2006). Indeed, Tapken et al. (2007) were able to measure a velocity shift between the interstellar absorption lines and the Lyα emission line for two of these objects, FDF1337 and FDF5550, because their UV continuum is bright. Both of them present a shift of ~600 km s^{-1} (cf. Table 1), a clear sign of outflows, which is most likely related to 3 times the expansion velocity of the shell as shown in Verhamme et al. (2006).

3.3.1. FDF1337 and FDF5550

To model FDF1337 and FDF5550, we have therefore fixed $V_{\rm exp} = 600/3 = 200$ km s^{-1}, and we proceed to adjust the 3 remaining shell parameters. Our best fits and the corresponding parameters are presented in Fig. 1. Note that both spectra are fitted with an intrinsic EW(Lyα)$_{\rm int}$ ~ 60 Å, which corresponds to the equilibrium value reached by a galaxy with constant star formation after 50−100 Myr (cf. Fig. 15). Even if the observed EW(Lyα)$_{\rm obs}$ is an order of magnitude lower, the intrinsic predicted EW(Lyα)$_{\rm int}$ seems to be "standard" in this sense. Dust (we find $\tau_{\rm a} = 1.0$ for 1337 and 1.5 for 5550, i.e. $E(B-V) \sim 0.1-0.15$) in a high neutral column density ($N_{\rm HI} = 5\times10^{20}$ cm^{-2}) outflow causes this attenuation. The derived Lyα escape fraction is $f_{\rm e} = 0.052$ for FDF5550 and $f_{\rm e} = 0.121$ for FDF1337. A rather small Doppler parameter, $b = 20$ km s^{-1}, is derived compared

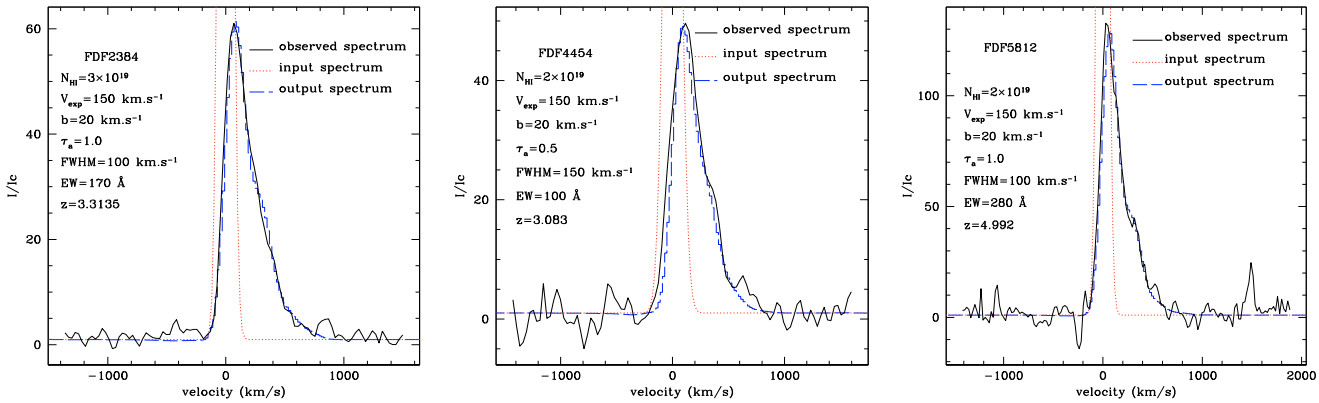

Fig. 2. Line profile fits for the three strongest Lyα emitters of the sample, presenting all a narrow asymmetric emission line: FDF2384 (*left*), FDF4454 (*middle*), and FDF5812 (*right*). Same symbols as figure in 1. The expansion velocity of the shell is $V_{\rm exp} \sim 150$ km s^{-1}, similar to the two precedent objects. The dust content is similar too, but $N_{\rm HI}$ is one order of magnitude lower. The intrinsic Lyα *EW* is also larger, particularly for FDF5812 ($EW({\rm Ly}\alpha)_{\rm int} = 280$ Å), but these values depend strongly on the continuum determination, which is quite uncertain for these faint objects. See text for more details.

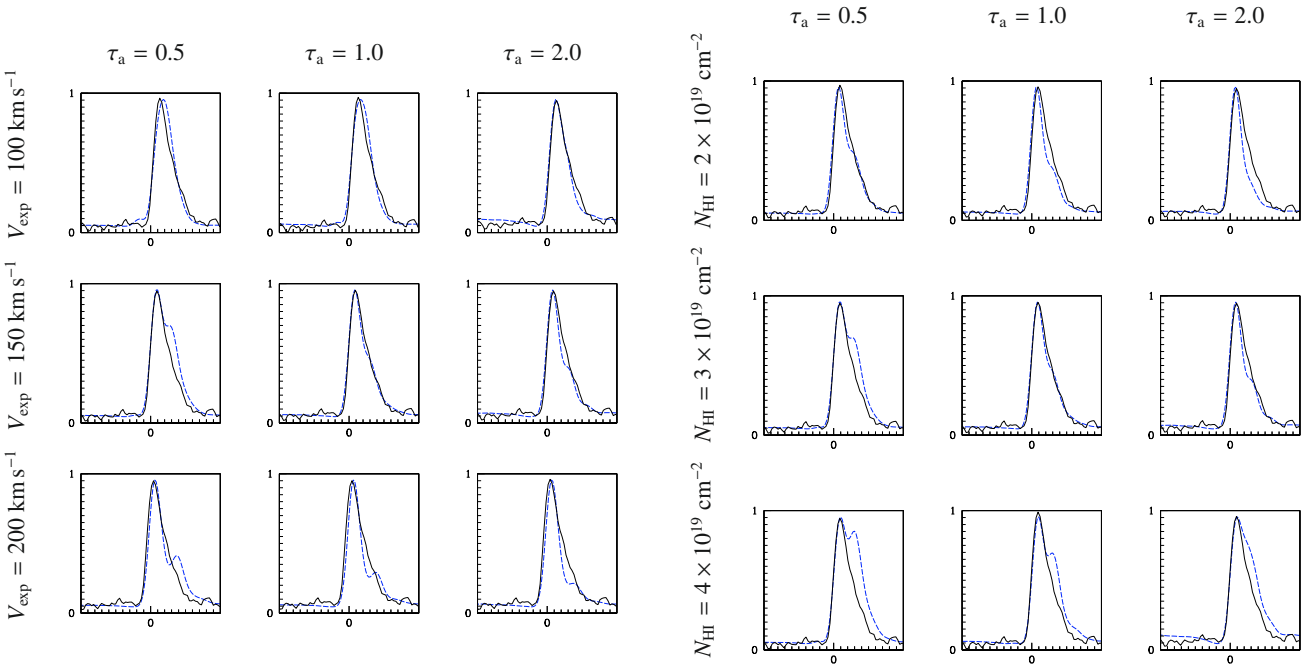

Fig. 3. Grid of predicted Lyα line profiles (blue dashed lines) compared to observed spectral line of FDF2384 to illustrate the constraints on the fit parameters $N_{\rm HI}$, $V_{\rm exp}$, and $\tau_{\rm a}$. All models have been computed with the same Doppler parameter ($b = 20$ km s^{-1}), and the same input spectrum (a flat continuum+a Gaussian emission line with $EW_{\rm int} = 80$ Å and $FWHM_{\rm int} = 100$ km s^{-1}). *Left* 3 × 3 *panel*: variations of $V_{\rm exp}$ (from 100 to 200 km s^{-1} from *top to bottom line*) and $\tau_{\rm a}$ (from 0.5 to 2.0 from *left to right*) for fixed $N_{\rm HI} = 3 \times 10^{19}$ cm^{-2}. *Right* 3 × 3 *panel*: variations of $N_{\rm HI}$ (from 2×10^{19} cm^{-2} to $N_{\rm HI} = 4 \times 10^{19}$ cm^{-2}) and $\tau_{\rm a}$ (from 0.5 to 2.0 from *left to right*) for fixed $V_{\rm exp} = 150$ km s^{-1}.

to cB58 ($b_{\rm cB58} = 70$ km s^{-1}) to reproduce the secondary peak on the elongated red wing. Note the extension of this red wing over ~1500 km s^{-1}.

3.3.2. FDF2384, FDF4454, and FDF5812

The Lyα fits for these objects are shown in Fig. 2. The profiles differ from the former by their high $EW({\rm Ly}\alpha)_{\rm obs} > 70$ Å, and a less extended red wing (~600 km s^{-1}). This leads to simulated neutral column densities an order of magnitude lower and higher escape fractions ($f_{\rm e} > 0.15$, cf. Table 2).

To illustrate how well constrained the model parameters are we will present in detail the fitting of the object FDF2384. In Fig. 3 a fraction of the model grid we use is shown for a fixed value $b = 20$ km s^{-1}, and for several values of $V_{\rm exp}$, $N_{\rm HI}$ and $\tau_{\rm a}$. The central profile of each 3 × 3 grid illustrates the best fitting profile for FDF2384. The observed profile of FDF2384 is overlayed on each cell. The overall behaviour of the spectra shown in this figure can be summarised as follows.

When $V_{\rm exp}$ increases, multi-peaks appear on the extended red wing. Indeed, the location of the second red-peak related to "backscattered" photons – photons which are reflected by the

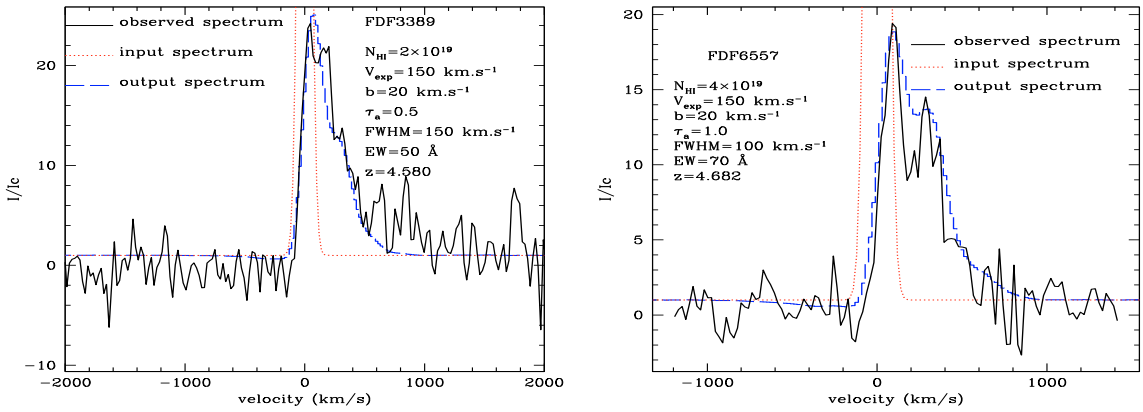

Fig. 4. Line profile fits for FDF3389 (*left*) and FDF6557 (*right*) showing asymmetric spectra with probable secondary structures on the red wing. Same symbols as in Fig. 1. The parameters derived from our fitting ($V_{\rm exp}$ = 150 km s^{-1}, $N_{\rm HI}$ ~ 2–4 × 10^{19} cm^{-2}, $\tau_{\rm a}$ = 0.5–1) are similar to the 3 narrow asymmetric cases (cf. Fig. 2) except for lower intrinsic *EW*, which here show values compatible with expectations for constant SFR over long timescales.

receding shell through the interior – is at $V_{\rm p} \sim 2V_{\rm exp}$, so when $V_{\rm exp}$ increases, the separation between this peak and the one at lower velocity (from the first-red-peak due to scatterings in the forthcoming part of the shell) increases (for more details, see Verhamme et al. 2006).

When $N_{\rm HI}$ increases, the "extension" of the Lyα line increases – the width between the sharp blue edge and the end of the red extended wing. Although very clear, this effect is relatively modest here, since $N_{\rm HI}$ changes only by a factor 2. This effect is easily understood by the increase of the optical depth in the medium, forcing Lyα to reach frequencies further from line center to escape.

When $\tau_{\rm a}$ increases, photons that undergo the highest number of scatterings will be destroyed, on average. This enhances the peaks made of back-scattered photons, whose escape is easier, thanks to this mechanism, than the escape of diffusing photons.

The Doppler parameter is fixed to b = 20 km s^{-1}, because higher values broaden the profiles too much, and secondary bumps are smoothed. Variations of b are discussed in Sect. 3.6.2.

The overall shape of the Lyα profile of FDF2384 is smooth, with a small bump visible in the extended red wing (at $V \sim$ 400 km s^{-1}); its position corresponds to $V_{\rm exp} \sim$ 150 km s^{-1}. Thanks to the "extension" of the line in FDF2384, we can fix $N_{\rm HI} \sim (2–4) \times 10^{19}$ cm^{-2}. Finally, the relative height of the bump compared to the main peak will determine correlated values for $N_{\rm HI}$ and $\tau_{\rm a}$, and two combinations are possible: ($N_{\rm HI} = 2 \times 10^{19}$ and $\tau_{\rm a} = 0.5$) provides a reasonable fit, but the best fit is obtained with ($N_{\rm HI} = 3 \times 10^{19}$ and $\tau_{\rm a} = 1.0$), as shown in Fig. 2.

The derived best fit escape fraction is $f_{\rm e} \sim 0.16$. There are large differences of the escape fraction, when $\tau_{\rm a}$ increases from 0.5 to 2, going from $f_{\rm e} \sim 40\%$ to $f_{\rm e} < 5\%$; correspondingly the intrinsic strength of the emission line varies from $EW_{\rm int} \sim$ 120 to 170 Å.

We proceed the same way to fit FDF4454 and FDF5812, which appear quite similar: the expanding shell has the same velocity $V_{\rm exp}$ = 150 km s^{-1}, the column density in the shell is an order of magnitude lower than in FDF1337 and FDF5550, but the dust amount, $\tau_{\rm a}$, remains the same. Since the intrinsic $EW({\rm Ly}\alpha)_{\rm int}$ is $\geq EW_{\rm obs}$ and the latter values are already relatively large, one obtains quite large intrinsic Lyα equivalent widths, between ~100 and 280 Å, for FDF2384, 4454, and 5812. The highest values require fairly young ages (see Fig. 15); however since these objects are quite faint, their continuum placement may be uncertain and $EW_{\rm int}$ may therefore be overestimated. The Lyα escape fraction of FDF4454 is high, $f_{\rm e} \sim 0.42$, because the shell is less dusty.

3.3.3. FDF3389 and FDF6557

These two objects are both at $z \sim 4.5$. They have medium observed equivalent widths ($EW({\rm Ly}\alpha)_{\rm obs}$ = 30–40 Å), compared to the former asymmetric profiles, and rather small extensions (~600–700 km s^{-1}). We treat them separately, because their spectra seem more complex than a smooth asymmetric emission line. They present multi-peaks on the red extension of the line. However, they are also more noisy, and these secondary features are only twice the noise amplitude. Nevertheless, we assume that they are significant, and we derive best-fits, taking these features into account (see Fig. 4).

The parameters derived from our fitting are close to the 3 narrow asymmetric cases ($V_{\rm exp}$ = 150 km s^{-1}, $N_{\rm HI} \sim 2–4 \times 10^{19}$ cm^{-2}, $\tau_{\rm a} = 0.5 – 1$) except for the intrinsic *EW*, which have "canonical" values – compatible with expectations for *SFR* = const. – again, because the observed *EW* are lower for these objects. The escape fraction is high for FDF3389 ($f_{\rm e}$ = 0.45), and lower for FDF6557 ($f_{\rm e}$ = 0.17) because of a higher column density and so a higher dust content.

3.4. The double-peaked Lyα profiles (group B)

Two of the 11 spectra present double-peaked profiles (FDF4691 and FDF7539). Such line morphologies are a natural outcome of radiation transfer in a static medium (Neufeld 1990), since in such media the Lyα photons can only escape by diffusing into the red or blue wings, where the opacity decreases rapidly.

3.4.1. FDF4691

This galaxy has a high $EW({\rm Ly}\alpha)_{\rm obs} \sim 80$ Å. Tapken et al. (2004) fitted this object with a code using a finite element method (Richling et al. 2001), and proposed $N_{\rm HI} = 4. \times 10^{17}$ cm^{-2} and b = 60 km s^{-1} in an almost static ($V_{\rm exp}$ = 12 km s^{-1}) and dust-free shell as best-fit parameters. The intrinsic spectrum they use is a Gaussian with *FWHM* = 1000 km s^{-1}, and no continuum. Using the same parameters we can reproduce their fit.

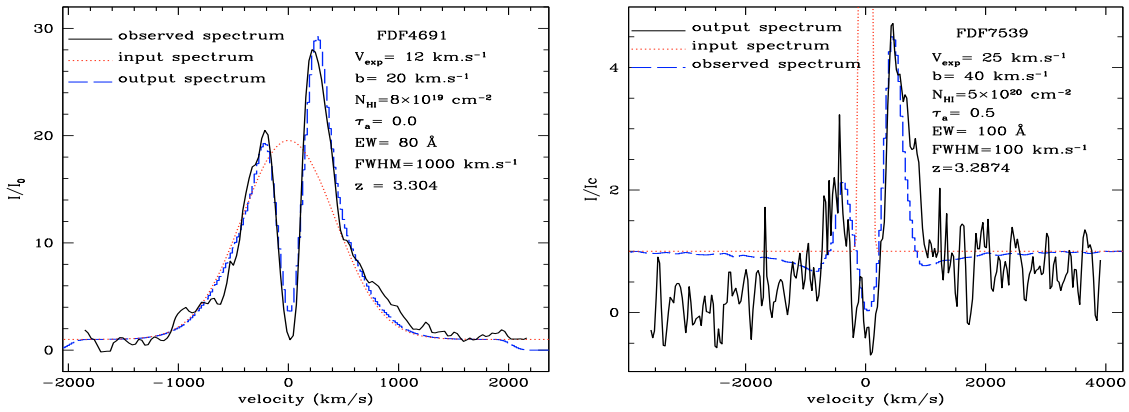

Fig. 5. Line profile fits for FDF4691 (*left*) and FDF7539 (*right*), the two double peaked profiles (type B) with static or almost static shells ($V_{\rm exp}$ = 10–25 km s^{-1}). The peak separation and the observed $EW(\mathrm{Ly}\alpha)_{\rm obs}$ are different for these objects, and so are the other fitting parameters. FDF4691 is the only object for which a very broad input spectrum is derived from the modelling ($FWHM$ = 1000 km s^{-1} instead of ∼100 for all other objects), possibly the signature of a hidden AGN.

However, since their code is not suited to high column densities we searched for other solutions. We find a fit of better quality – the deep gap between the peaks is better reproduced by a smaller b, and the red wing is fitted with more accuracy starting from an input spectrum with a continuum – with a higher column density ($N_{\rm HI} = 8 \times 10^{19}$ cm^{-2}), and consequently a smaller b = 20 km s^{-1}[1] (see Fig. 5 for the fit and Table 2 for a summary of the parameters). Our best fit is obtained with no dust, and the fit with $\tau_{\rm a} = 0.1$ is less good than the one with no dust, from which we estimate an upper limit on the dust content of $\tau_{\rm a} \lesssim 0.1$. This is consistent with the fact that the Lyα and UV SFR indicators derived from observations (Tapken et al. 2007) are similar. To reproduce the very extended wings of the line, the intrinsic Lyα emission line has to be very broad. It is characterised by a very large value of $FWHM_{\rm int}$ = 1000 km s^{-1}, and a "st andard" $EW(\mathrm{Ly}\alpha)_{\rm int}$ = 90 Å. Radiation transfer effects are inefficient to broaden the line in a medium with such a low column density. If interpreted as a result of virial motion, such a large $FWHM$ seems, however, unphysical. A hidden AGN may be an explanation for the high $FWHM$, as suggested by Tapken (2005).

A solution to reproduce the observed spectrum with a more realistic intrinsic spectrum ($FWHM_{\rm int}$ = 100 km s^{-1} and $EW_{\rm int}$ = 80 Å) is to invoke two contributions from two different media: when we sum emergent spectra from two identical shells except for the column density (b = 20 km s^{-1}, $V_{\rm exp}$ = 10 km s^{-1}, no dust, $EW(\mathrm{Ly}\alpha)_{\rm int}$ = 80 Å, and $nh = 4. \times 10^{17}$ cm^{-2} for one and $N_{\rm HI} = 4. \times 10^{20}$ cm^{-2} for the other), we are able to reproduce a spectrum with narrow peaks close to the center and broad wings, starting from a "standard" value for the $FWHM$, $FWHM(\mathrm{Ly}\alpha)_{\rm int}$ = 100 instead of 1000 km s^{-1} (see Fig. 6). This could correspond to a physical situation where an initially thick shell has been stretched until a hole forms, and the diffuse medium in the hole is still opaque enough to imprint radiative transfer effects on Lyα photons. The surfaces of the thick shell and the hole are of equal size in this first model. The parameters listed for FDF4691 in Table 2 are those of the homogeneous single shell model discussed above.

[1] Indeed, the location of the peaks were predicted in static media, and depend on a combination of $N_{\rm HI}$ and b.

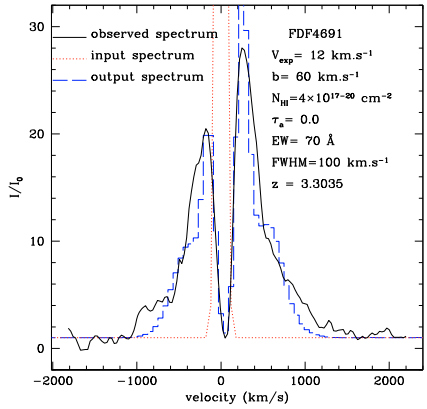

Fig. 6. Fit of FDF4691 with a "two-phase" model, a low density shell with $N_{\rm HI} = 4. \times 10^{17}$ cm^{-2} and a high density shell with $N_{\rm HI} = 4. \times 10^{20}$ cm^{-2}. The other parameters of the shells are identical: b = 60 km s^{-1}, $V_{\rm exp}$ = 12 km s^{-1}, no dust, $EW(\mathrm{Ly}\alpha)_{\rm int}$ = 70 Å. This allows for a more reasonable $FWHM(\mathrm{Ly}\alpha)_{\rm int}$ = 100 km s^{-1} instead of 1000.

3.4.2. FDF7539

For this object the velocity shift between the LIS in absorption and Lyα in emission was measured: Δv(em – abs) = 80 km s^{-1}, which implies a shell velocity $V_{\rm exp} = 80/3 \sim 27$ km s^{-1}, i.e. almost static as in the case of FDF4691, or at maximum ≲40 km s^{-1}, in the case of a low column density. Indeed, the spectrum is also double-peaked as for FDF4691.

The large peaks separation ($V_{\rm p} \pm 500$ km s^{-1}, larger than for FDF4691) implies a high column density. Presumably, the rather low observed $EW(\mathrm{Ly}\alpha)_{\rm obs}$ also implies the presence of dust in the shell. Indeed, the best fit shown in Fig. 5 has a high column density ($N_{\rm HI} = 5 \times 10^{20}$ cm^{-2}), and dust ($\tau_{\rm a} = 0.3$). It is compatible with the canonical value for the intrinsic Lyα spectrum. The resulting escape fraction is $f_{\rm e} = 0.28$.

For comparison, Tapken et al. (2007) proposed a fit of similar quality for this object, but the velocity of the shell they derive from their modelling is high ($V_{\rm exp}$ = 190 km s^{-1}), which is in contradiction to the observed small velocity shift between Lyα and LIS (Δv(em – abs) = 80 km s^{-1}), and surprising for a double-peaked profile. As their investigation is restricted to low column densities, the only solution they have to produce

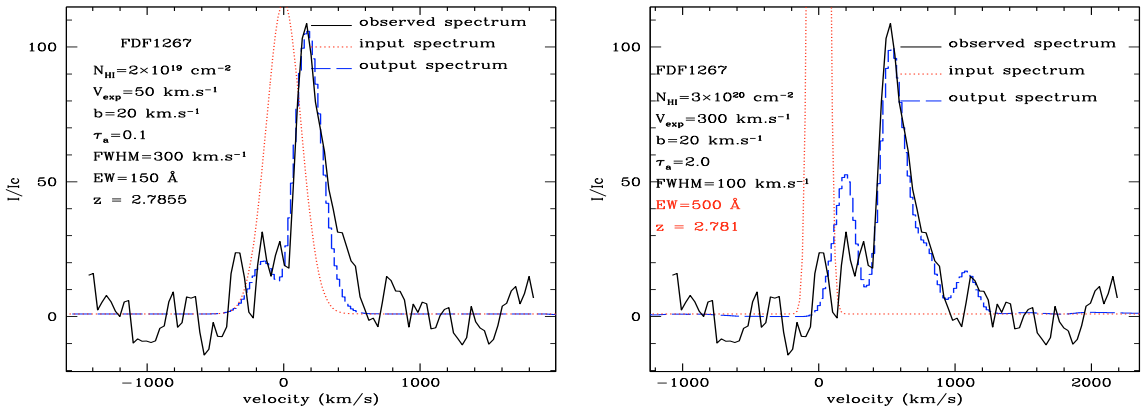

Fig. 7. Fitting FDF1267 with two different scenarios: the bump is either considered as a blue peak in an almost static shell (*left*), or as the first red peak of Lyα emission (*right*).

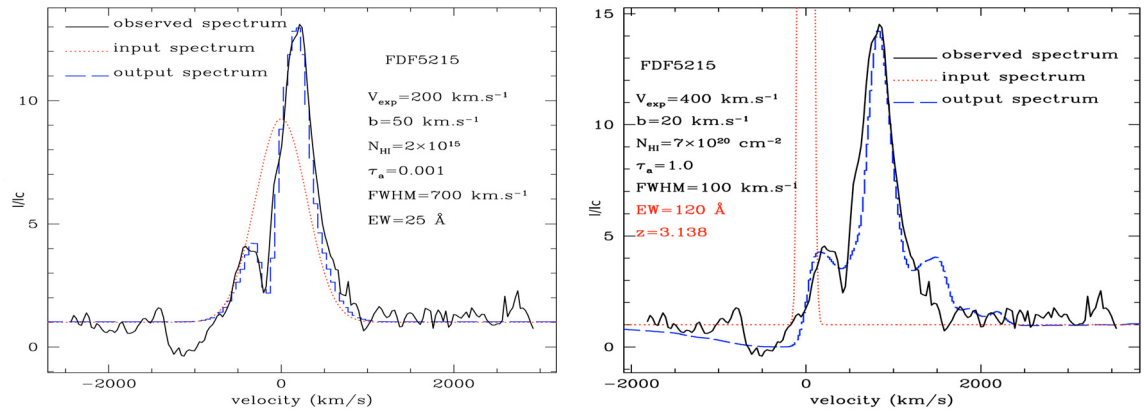

Fig. 8. Fitting FDF5215 with two different scenarios: the bump is either considered as a blue peak in an almost static shell (*left*), or as the first red peak of Lyα emission (*right*).

separated and broad peaks is with high values of $V_{\rm exp}$ and b, and a huge intrinsic $FWHM$ (∼1900 km s^{-1}).

3.5. Other Lyα profiles (group C)

3.5.1. FDF1267

This object presents an asymmetric emission peak plus a bump on the blue side of this peak with a strong observed $EW({\rm Ly}\alpha)_{\rm obs}$ = 129 Å. The Lyα profile, shown in Fig. 7, can be fitted by different scenarios. On the left panel of Fig. 7, the bump is considered as a blue peak in an almost static ($V_{\rm exp}$ = 50 km s^{-1}) shell with a low column density ($N_{\rm HI}$ = 2×10^{19} cm^{-2}) and a small amount of dust ($\tau_{\rm a}$ = 0.1). Values of b higher than b = 20 km s^{-1} lead to too separated peaks. The escape fraction is $f_{\rm e}$ = 0.6352. On the right panel, we fit the profile with a fast moving ($V_{\rm exp}$ = 300 km s^{-1}), dense ($N_{\rm HI}$ = 3 × 10^{20} cm^{-2}) and dusty($\tau_{\rm a}$ = 2.0) shell, leading to $f_{\rm e}$ = 0.02, and a very large intrinsic $EW({\rm Ly}\alpha)_{\rm int}$ = 500 Å. Dust is needed in this configuration to reproduce narrow and well separated peaks. Indeed, dust more efficiently destroys photons that undergo the highest number of scatterings, i.e. all but the backscattered photons, which "isolates" and "slims down" the peaks. Note that this solution requires an adjustment of the source redshift to $z \sim 2.781$ instead of $z \sim 2.788 \pm 0.001$ derived by Tapken et al. (2007). However, this object is the only one for which the redshift determination is only based on Lyα, so so far this poses no difficulty.

Our favoured solution is the "quasi-static shell" picture. Indeed, the high $EW_{\rm int}$ inferred in the second fit seems unlikely. Furthermore, the large observed $EW_{\rm obs}$ of 1267 would imply a rather low column density as discussed in Sect. 4.2.1. Finally, the SFR values derived from uncorrected UV and Lyα fluxes (SFR(Lyα) > SFR(UV)) indicate a low dust content. An accurate redshift measurement of FDF1267, independent of Lyα, should allow us to distinguish between these two solutions.

3.5.2. FDF5215

FDF5215, shown in Fig. 8, presents the same spectral shape as FDF1267: a small bump on the blue side of the asymmetric strong emission, but the noise level is much lower, and this small bump has to be taken into account. Again, two different scenarios can reproduce the spectral shape. The bump is either considered as a blue peak in an almost static shell, or as the first red peak of Lyα emission. The two solutions, differing by more than 5 orders of magnitude in $N_{\rm HI}$, are listed in Table 2. FDF5215 was also modeled by Tapken et al. (2007); their set of parameters is similar to our solution at low $N_{\rm HI}$, except for a higher value of b.

None of our fits is really satisfying. The solution at low-$N_{\rm HI}$ (left panel) well reproduces the observed profile, but the derived column density is very low: at least 4 orders of magnitude lower than the rest of the sample. As a consequence, the $FWHM$ of the intrinsic Lyα emission is huge ($FWHM$ = 700 km s^{-1}) to reproduce a broad profile without efficient broadening due to radiation transfer in an almost transparent medium. Finally, this

solution does not reproduce the absorption at $V = -1200$ km s^{-1} discussed below. On the other hand, the solution with high $N_{\rm HI}$ and a standard intrinsic *FWHM* fits less well. Furthermore, the redshift derived from this fit is out of the error bars ($z = 3.138$ instead of 3.148 ± 0.004).

The black absorption component, found at $V \sim -1200$ km s^{-1} in this object (see Fig. 8 left), is unaccounted for in the fit with low $N_{\rm HI}$. How likely is it that this represents a chance alignment of an H I absorber? If fitted separately with a Voigt profile the absorption is well described by $b \sim 70$ km s^{-1}, and $N_{\rm HI}$(abs) $\sim 2 \times 10^{17}$ cm^{-2}. Using the column density distribution from Misawa et al. (2007) we find that the probability of finding an absorber with $>N_{\rm HI}$(abs) in a velocity interval of say 4000 km s^{-1} is ∼5%. It seems thus more likely that this feature is related to the galaxy. We conclude that none of our solutions is clearly favoured, and further observations are needed to help constrain the models for FDF5215.

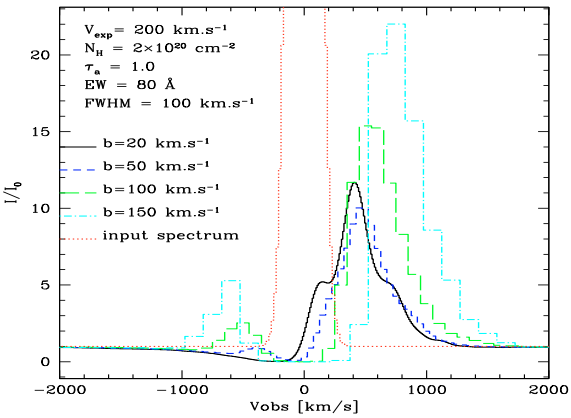

Fig. 9. Dependence of the Lyα line profile on b for typical shell parameters. Note the shift of the red peak with increasing b, and the emergence of a blue counterpart. The escape fraction also increases with b.

3.6. Uncertainties and degeneracies in Lyα fits

3.6.1. Uncertainties on each parameter

The parameters listed in Table 2 correspond to best-fits determined by eye, without resorting to minimisation techniques. We now attempt to indicate the approximate uncertainties of the derived parameters.

The characteristic uncertainty on the expansion velocity is estimated to be ∼50 km s^{-1}, which is the step in velocity in our grid of models. The sampling in $\tau_{\rm a}$, the dust absorption optical depth, is not linear (we have assumed $\tau_{\rm a}$ values of 0, 0.1, 0.5, 1, 2, 3, and 4 for our grid), but it was refined when necessary. From the line fits the characteristic uncertainties on $\tau_{\rm a}$ and on the neutral column density $N_{\rm HI}$ are estimated as ±50%. We refer to Fig. 3 for an idea of the uncertainties on $N_{\rm HI}$ and $\tau_{\rm a}$. Other comparisons, e.g. with SED fits and by imposing a consistency between different SFR indicators, indicate that the uncertainty on the extinction may be somewhat larger, up to a factor ∼2 in some cases (see Sect. 4.8).

The Doppler parameter is set to the default value $b = 20$ km s^{-1}, which allows us to reproduce the relative narrow peaks observed, and secondary features on the extended red wing of the profiles. Models were computed for other values of b (10, 20, 40, 80, and 200 km s^{-1}), but did not lead to better fits. We estimate the uncertainty on this parameter at around 50%.

The uncertainty on the intrinsic equivalent width can be fairly large, and it mostly depends on the determination of the continuum. Indeed, for strong Lyα emitters, like FDF5812, the continuum is so weak that it is poorly constrained, and the uncertainty on the continuum level is around 20%. As already mentioned, all the spectra presented above have been normalized to the same level as determined by Tapken et al. (2007) to derive observed Lyα $EW_{\rm obs}$. However, choosing the continuum level by eye we may also obtain acceptable solutions with lower intrinsic $EW({\rm Ly}\alpha)_{\rm int} \sim 80$ Å for the three stronger Lyα emitters (FDF2384, FDF4454 and FDF5812), in better agreement with a scenario of constant star formation over ∼100 Myr. Only for FDF1267 do all solutions seem to imply a fairly high intrinsic Lyα equivalent width.

The intrinsic *FWHM* was set to $FWHM = 100$ km s^{-1} as a default value, and good fits were obtained for almost all spectra; exceptions are the very low $N_{\rm HI}$ solution for FDF5215 and the very broad double-peaked profile of FDF4691 (except if we consider a shell with two components as described before).

3.6.2. Degeneracies

Although degeneracies in principle affect our profile fits, it turns out that asymmetric line profiles provide fairly non-degenerate solutions. We briefly describe how the influence of the main parameters (b, $N_{\rm HI}$, $V_{\rm exp}$, *FWHM*, and $\tau_{\rm a}$) can be discerned.

Doppler parameter *b*: After several attempts to fit the data with large values b (>50 km s^{-1}), we adopted a typical value $b = 20$ km s^{-1}. The Doppler parameter has a complex influence on the Lyα profile: small b lead to asymmetric emission lines on which the potential multi-peaks due to a high expansion velocity would be visible (see Fig. 3). Large values of b (>50 km s^{-1}) lead to a smoothed red peak (the multi-peaks are not visible any longer), whose location is redshifted. Furthermore a blue emission component appears whose strength increases with b, reproducing a kind of "double-peaked profile" as in static media, but with asymmetric peaks – the two sides of each peak do not have the same slope (see Fig. 9) – even in shells with high velocities ($V_{\rm exp} > 200$ km s^{-1}).

In our sample, the spectra from group A (asymmetric profiles) do not show blue components, and faint multi-peaks (bumps on the extended wing) may be visible. Therefore low values of b (=20 km s^{-1}) are required to fit our spectra. On the contrary, other spectral types (B and C) may be fitted with larger values of b.

Column density $N_{\rm HI}$: With increasing neutral hydrogen column density, the blue edge of the Lyα emission is progressively redshifted with respect to the systemic galaxy redshift. Thus, if z is known accurately enough, the neutral column density in the shell is well constrained. The full width of the line increases with increasing $N_{\rm HI}$ too. Indeed, it is impossible to fit narrow lines ($FWHM < 500$ km s^{-1}) with high column densities ($N_{\rm HI} > 10^{20}$ cm^{-2}), and extended lines ($FWHM > 500$ km s^{-1}) with low column densities ($N_{\rm HI} < 10^{20}$ cm^{-2}), if the expanding shell model applies (cf. Sect. 4.6 and Fig. 13).

Expansion velocity: The overall shape of the line profile – presence of secondary peaks or not – constrains the velocity of the shell: fast moving shells ($V_{\rm exp} > 200$ km s^{-1}) lead to multi-peaks in the Lyα profile, whereas static or almost static shells lead to double-peaked profiles with symmetrical peaks – the two sides of each peak have the same slope.

Dust content: Finally, the dust content is adjusted to fit the peak width and the relative height of the bumps – if any – compared to the main peak.

In conclusion, few degeneracies appear in the modeling of asymmetric Lyα line profiles (group A). Thanks to the location of the blue edge and to the full width of the line $N_{\rm HI}$ is well constrained for asymmetric spectra. Furthermore, the global line shape (one single peak) implies low values of b (<50 km s^{-1}) and $V_{\rm exp}$ (<250 km s^{-1}). On the contrary, the 4 spectra with more complex profiles (1267, 5215, 4691 and 7539) present degeneracies. Tapken et al. (2007) proposed Lyα fits for 3 of them (4691, 5215, 7539). We can reproduce their fits, but propose fits with other sets of parameters, as our code allows for higher column densities than the code Tapken et al. (2007) used. Automated fitting methods and a thorough examination of the uncertainties and possible degeneracies in Lyα line profile fits will be useful in the near future, when larger samples of spectra of sufficient S/N and resolution become available.

3.6.3. Possible limitations of the model

As described in Sect. 2, our modeling makes some simplifying assumptions, including in particular the geometry and the homogeneity of the shell. How far these assumptions would alter our results is presently unclear and remains to be explored in the future.

Inhomogeneous/clumpy geometries have e.g. been explored by Hansen & Oh (2006); the line profiles obtained from such models do not seem to change significantly. However, how much our model parameters would be modified remains to be examined. For the time being it seems clear that few if any cases are know where clumpy geometries would favour Lyα transmission over the continuum (cf. Neufeld 1991; Hansen & Oh 2006). This can e.g. be concluded from the comparison of Hα and Lyα in local starbursts (Atek et al. 2008), and from the comparison of UV and Lyα SFR indicators. Indications for one possible case of such Lyα boosting have been found among 4 objects analysed by Finkelstein et al. (2007a). Other geometries have e.g. been considered in Paper II, where deviations from the constant velocity shell have been necessary for the analysis of cB58.

The effect of the intergalactic medium (IGM) has been neglected in our approach. Even if the IGM is almost fully ionised at $z \sim 3$, the redshift of the bulk of our objects, the effect of the intervening Lyα forest corresponds statistically to a transmission of ~70 and 40% ($\tau_{\rm eff} \sim 0.3-1$) between $z \sim 3$ and 4 (Faucher-Giguere et al. 2007). In our modeling we find no need to account for such an IGM reduction within ~1000−2000 km s^{-1} of the Lyα line; not even in the two highest redshift ($z \sim 4.7-5$) objects. No individual Lyα forest absorption components are found in this interval; furthermore for most objects, except possibly FDF 1337, 5550, 7539, and maybe also 3389, the predicted continuum flux blueward of Lyα agrees within the uncertainties with the observed continuum. In any case, less importance has been given to the line fits on the blue side of Lyα. Also, in a detailed analysis of the Lyα forest along the line of sight of the $z \sim 2.7$ LBG cB58, Savaglio et al. (2002) found no indication for neutral gas within ~4000 km s^{-1} of the systemic velocity of the galaxy. From these considerations we conclude that our Lyα line fits are probably unaffected by additional matter beyond the expanding shell included in our models.

4. Discussion and implications from our model fits

We now discuss the values of the parameters determined for the 11 objects, possible correlations among them, and we compare them with other measurements from the literature.

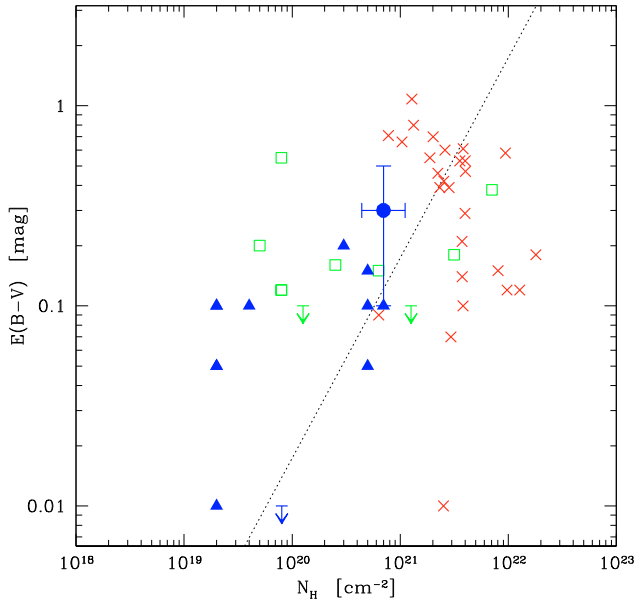

Fig. 10. Comparison of gas extinction, $E(B-V)$, and H I column density for the FDF objects (blue triangles), cB58 (blue error bar), local starbursts from Calzetti (2007, private communication, red crosses), and measurements from the nearby starbursts analysed by Kunth et al. (1998) (green squares). The multiple solutions for the FDF objects are also plotted except for low $N_{\rm HI}$ solution of FDF5215; for FDF4691 an arbitrary upper limit of $E(B-V) < 0.01$ is adopted in the plot. The mean Galactic relation $N_{\rm H}/E(B-V) = 5.8 \times 10^{21}$ cm^{-2} mag^{-1} from Bohlin et al. (1978) is indicated by the dotted line.

4.1. The neutral column density

The neutral column density we derive from the fitting of 11 Lyα spectra from the FORS Deep Field is radial – along a line of sight, from the center of the shell to the end of the simulation volume – and ranges over more than an order of magnitude, from $N_{\rm HI} = 2. \times 10^{19}$ to $N_{\rm HI} = 5. \times 10^{20}$ cm^{-2}. However, the majority of objects have a low column density (8/11 have $N_{\rm HI} < 1. \times 10^{20}$ cm^{-2}).

How do our $N_{\rm HI}$ determinations from Lyα fitting compare with other $N_{\rm HI}$ determinations in starbursts? Carrying out such a comparison is difficult for LBGs, since H I column densities are usually not measured. Even for nearby starbursts the available data is scarce. Calzetti (2007, private communication) has kindly determined $N_{\rm HI}$ for us from published 21 cm RC3 radio observations and assuming sizes given by D_{25}[2]. For comparison we have also compiled $N_{\rm HI}$ and $E(B-V)$ measurements from the small sample of nearby starbursts observed in the Lyα region by Kunth et al. (1998). These comparison samples are plotted in Fig. 10. For SBS 0335-052 we have added a second point, adopting $N_{\rm HI}$ from Thuan & Izotov (1997) and the extinction from Atek et al. (2008). Similarly two points are shown for IRAS08339+6517 using the extinction compiled by Kunth et al. (1998) and the one measured by Atek et al.

Despite some overlap, $N_{\rm HI}$ is lower in our objects than the column density observed by Calzetti and collaborators, and more similar to the small sample of Kunth et al. An attempt to explain this can be the different ways of determining $N_{\rm HI}$: for the Calzetti sample the determination of the neutral column density was achieved by radio observations of the whole galaxy, whereas in the case of Kunth et al., $N_{\rm HI}$ is derived from Voigt fitting of the

[2] The radii obtained in this way reach from ~5 to 50 kpc, with a median around 17 kpc.

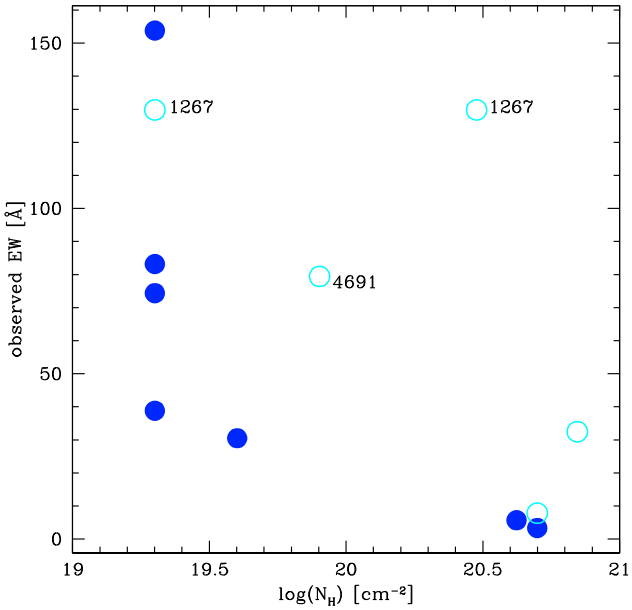

Fig. 11. Observed Lyα $EW_{\rm obs}$ versus derived radial H I column density. The three objects with the lowest $EW_{\rm obs}$ are artificially displaced by a small amount for illustration purposes. We may see an anticorrelation between the observed Lyα $EW_{\rm obs}$ and the neutral column density in the shell, for the 11 objects from the FDF, if we eliminate the high-$N_{\rm HI}$ solutions for 1267, and the very low-$N_{\rm HI}$ solution for 5215. The filled circles are objects presenting asymmetric profiles (type A), the open circles are the others (type B, C). The quasi-static object 4691 with a double-peaked profile stands out from this trend for unknown reasons.

Lyα profile, so it only takes into account the neutral gas which influences Lyα radiation transfer, even if a Voigt fitting may lead to an underestimate of $N_{\rm HI}$ (Verhamme et al. 2006, see Sect. 4). This may explain why the determination from Kunth et al. is closer to our values than those of Calzetti et al. In any case, to compare our column densities with those of Calzetti one needs to increase our $N_{\rm HI}$ values typically by a factor ∼2 to convert the radial shell column density to a total one.

The range of $N_{\rm HI}$ found for the FDF objects is also compatible with our confirmation of the neutral column density of the gravitationally lensed $z \sim 3$ LBG MS1215-cB58 (cB58, shown as the blue cross) that we fitted previously (Paper II). Indeed, $N_{\rm HI}$(cB58) $\sim 7. \times 10^{20}$ cm^{-2} is slightly higher than $N_{\rm HI}$ of the FDF Lyα emitters, as expected for a Lyα spectrum in absorption.

4.2. Lyα equivalent widths

4.2.1. Observed *EW*s

The observed Lyα *EW*s range from 6 to 150 Å in the rest frame. Does this range reflect intrinsic differences, or is it related to the physical conditions of the ISM in which Lyα radiation transfer takes place? We examined how $EW_{\rm obs}$ correlates with other parameters, but no clear correlation is seen. We found a trend in $EW_{\rm obs}$ with respect to the neutral column density in the shell (see Fig. 11): $EW_{\rm obs}$ seems to decrease with $N_{\rm HI}$, at least for the asymmetric profiles (filled circles). In fact, the objects with a low $EW_{\rm obs}$ (<10 Å, i.e. FDF1337, 5550, and 7539) can only be fitted with a high value of $N_{\rm HI}$, since their profiles are very broad. On the other hand, narrow lines with large $EW_{\rm obs}$ can only fitted with small values of $N_{\rm HI}$. There may be three exceptions to this trend, FDF4691, 5215, and 1267. The double-peaked profile of 4691 seems peculiar, as it is static and dust-free, as suggested by the *SFR*(UV) and *SFR*(Lyα) which are almost identical. We imagine that this trend breaks down in dust-free media, or in media with a very small amount of dust, because dust is needed to absorb radiation and decrease the intrinsic $EW_{\rm int}$ value. FDF1267 and 5215 are peculiar/degenerate for the reasons discussed above (Sect. 3).

An anti-correlation of $EW_{\rm obs}$ vs $N_{\rm HI}$ can be understood by radiation transfer effects if the intrinsic $EW_{\rm int}$ is approximately constant. When $N_{\rm HI}$ increases, the path length of Lyα photons increases, and so does their chance of being absorbed by dust: the Lyα escape fraction decreases with increasing $N_{\rm HI}$, as mentioned above. Furthermore, if we assume a constant dust-to-gas ratio, an increase in $N_{\rm HI}$ naturally leads to an increase of the dust quantity (the optical depth). These two effects explain the decrease of the observed Lyα *EW* with increasing $N_{\rm HI}$ from a theoretical point of view.

4.2.2. Intrinsic *EW*s

Three objects (2384, 5812, 1267) have very large intrinsic $EW({\rm Ly}\alpha)_{\rm int} > 100$ Å; for one (5215) the two solutions give quite disparate results, and the remaining 7 objects all have intrinsic $EW_{\rm int}$ of ∼50−100 Å. Taking the uncertainties in the continuum placement into account (cf. above) we consider that this latter group (7 of 11 objects) have intrinsic $EW({\rm Ly}\alpha)_{\rm int}$ compatible with expectations for star-forming galaxies with a constant star formation history over periods ≳10−100 Myr, as seen in Fig. 15. The strength of Lyα in three high $EW_{\rm obs}$ objects implies younger ages, irrespectively of their star formation history.

4.3. Dust extinction

We have derived here for the first time constraints on the dust content of galaxies using the Lyα profile only. It is therefore of interest to examine how this determination compares with other methods.

Using a version of the SED fit and photometric redshift code *Hyperz* described in Schaerer & Pelló (2005) and the *UBgRIJK*s photometry published by Heidt et al. (2003), we have modeled the SED of our objects, assuming the Calzetti attenuation law (Calzetti et al. 2000). Three objects, 5812, 3389, and 6557, have insufficient data (photometry in 3 or less bands) which does not allow meaningful SED fits. 2384 is also excluded, since it appears to be a multiple source, where the Lyα emission is clearly displaced from the continuum. Results for the remaining objects are shown in Fig. 12, where we compare the extinction derived assuming models with constant star formation (red filled triangles) or exponentially decreasing SF histories (blue open circles) described by the Bruzual & Charlot templates with $E(B-V)$ derived from our Lyα line fits. Note that these values, denoted here as $E(B-V)^\star$(Hyperz), measure the extinction undergone by the stars, whereas $E(B-V)({\rm Ly}\alpha)$ measures that of the Lyα emitting gas. The two may differ, as has been seen in local starbursts between the stellar extinction and the one measured from the Balmer decrement (Calzetti et al. 2000).

Figure 12 shows the good correlation between the different extinction measures, especially when different SF histories are allowed for. Indeed, for the bulk of the objects the extinction derived from Lyα profile fitting is between the gas extinction expected from Calzetti's empirical relation, $E(B-V)^{\rm gas} = 1/0.44E(B-V)^\star$, and a somewhat lower value of $E(B-V)^{\rm gas}$.

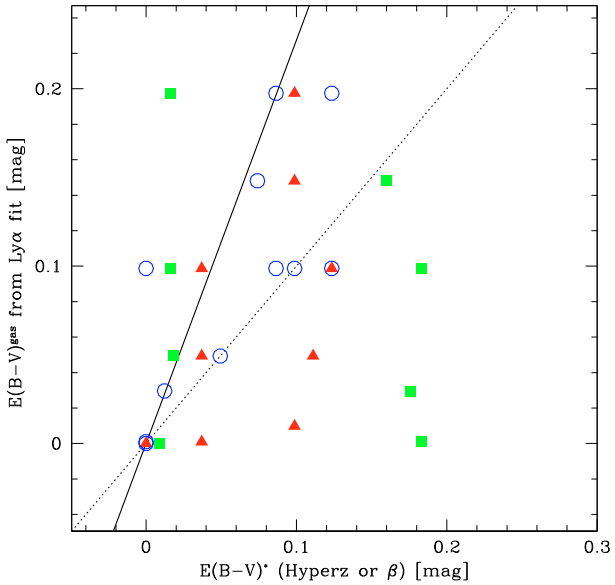

Fig. 12. Comparison of the extinction $E(B-V)$ determined from the Lyα profile fits versus other methods for objects with sufficient photometry and/or measured β slopes. Multiple solutions from Lyα fits are included. *Hyperz* SED fits using constant SFR models (red filled triangles) or arbitrary SF histories (blue open circles). Green squares show values of $E(B-V)^{\rm gas}$ determined from the β-slope. The dotted line shows the one-to-one relation, the solid line the relation $E(B-V)^{\star} = 0.44E(B-V)^{\rm gas}$ found empirically (cf. Calzetti et al. 2000).

We can also estimate the extinction from the UV slope, β. Excluding again the multiple source 2384, the observed UV slopes show two groups, whose extinctions, estimated following Calzetti et al. (2000), are $E(B-V)^{\star} \sim 0.-0.02$ and 0.16–0.18 shown by the green squares in Fig. 12. These values cover a similar range as $E(B-V)^{\star}$(Hyperz), although with a poor correlation. This could be due to the statistical nature of the underlying correlation between attenuation and β. We conclude that overall Lyα line profile fits allow us to obtain fairly consistent extinction values compared to broad band photometry fits of the individual objects. Our derived extinction values, corresponding to $E(B-V) \sim 0-0.2$, are also in good agreement with the values found for LBGs by Shapley et al. (2003) and others (e.g. Papovich et al. 2001).

4.4. Gas to dust ratio

How do the gas-to-dust ratios obtained from our line profile fits compare with other values observed in starbursts? To address this we return to our comparison samples shown in Fig. 10.

Compared to the Galactic average of $N_{\rm HI}/E(B-V) = 5.8 \times 10^{21}$ cm^{-2} mag^{-1} and its ∼30% scatter (cf. Bohlin et al. 1978), our results show somewhat lower gas-to-dust ratios and seemingly a larger scatter. The scatter is, however, similar to the one found among the local starbursts also shown in this figure. Pettini et al. (2000) noted this difference in the gas-to-dust ratio for cB58, which they suggest could indicate that a significant fraction of the gas is not in atomic form, i.e. is either ionised and/or in molecular hydrogen.

The Calzetti objects have a median of $N_{\rm HI}/E(B-V) = 7.9 \times 10^{21}$ similar to the "classical" Galactic value but showing a wide dispersion. Approximately half of our objects show $N_{\rm HI}/E(B-V)$ values lower than those of Calzetti's local starbursts. For the other half of the sample, and for the LBG cB58 modeled in Paper II, the values of the gas-to-dust ratio overlap with those for the Calzetti sample. The comparison may be hampered for the reasons also affecting the $N_{\rm HI}$ comparison (cf. Sect. 4.1). Overall we conclude that the gas-to-dust ratios determined purely from Lyα line profile fitting yield values consistent with those of local starbursts or somewhat lower. For comparison, Vladilo et al. (2007) find higher gas-to-dust ratios in DLAs compared to the Galactic value.

If some LBGs show truly lower gas-to-dust ratios, this may be due to a higher degree of metal enrichment in the outflowing H I gas, and/or an overall smaller fraction of neutral gas being "polluted" in nearby starbursts, and/or a smaller fraction of atomic hydrogen. However, the column densities found in LBGs are also consistently lower than in local starbursts (cf. Fig. 10), which may indicate a different "regime". Other, independent determinations of the gas-to-dust ratio in LBGs and other starbursts and more detailed examinations would be required to clarify these issues and to understand the possible physical causes for such differences.

4.5. Velocity of the outflow

Assuming a galaxy-scale outflow surrounding our 11 objects (the relevance of this model is discussed in Sect. 2), we have derived the expansion velocity $V_{\rm exp}$ of the shell from the Lyα spectral shape for 8 objects, and deduced it for the 3 other objects (1337, 5550, 7539) from the measurement of the shift between the LIS absorption lines and the Lyα emission. Overall 9 objects out of 11 have shell velocities around 150–200 km s^{-1}, and 2 objects present almost static shells. No correlation between the expansion velocity and other parameters is found. We now briefly discuss the high velocity outflows and the few nearly static cases. However, we have no explanation for the low ISM velocity cases: we do not know why these objects are different from the more common cases showing outflows.

4.5.1. High velocity objects

All objects presenting an asymmetric emission line are reproduced with $V_{\rm exp} \sim 150-200$ km s^{-1}. This velocity range is very similar to the determination of Shapley et al. (2003), from the blueshift of LIS absorption lines with respect to stellar lines in a sample of ∼800 LBGs at redshift $z \sim 3$, as well as in cB58, where the outflow velocity is estimated as $V_{\rm exp} = 255$ km s^{-1} (Pettini et al. 2002).

Two objects with a more peculiar spectral shape, FDF 1267 and 5215, can also be fitted with higher expansion velocities ($V_{\rm exp} \sim 400$ km s^{-1}), a high $N_{\rm HI}$, and high dust content. However, 1267 has such a large observed equivalent width ($EW_{\rm obs} = 129$ Å) that it may rather have a small column density to fit better in the plot showing a correlation between the observed Lyα $EW_{\rm obs}$ and $N_{\rm HI}$ (see Fig. 11). This peculiar spectral shape is also found in observations of an LBG at redshift $z \sim 3.7$ by Vanzella et al. (2008) in the GOODS-South field.

4.5.2. Low velocity objects

The two double-peaked spectra (4691 and 7539) are characterised by a static (or almost static, $V_{\rm exp} < 25$ km s^{-1}) surrounding shell. In the case of 7539, the velocity shift between the LIS absorption lines and Lyα is known (Δv(em – abs) = 80 km s^{-1}), so the shell velocity is an observational constraint ($V_{\rm exp} \sim \Delta v$(em – abs)/3). This peculiar spectral shape (double

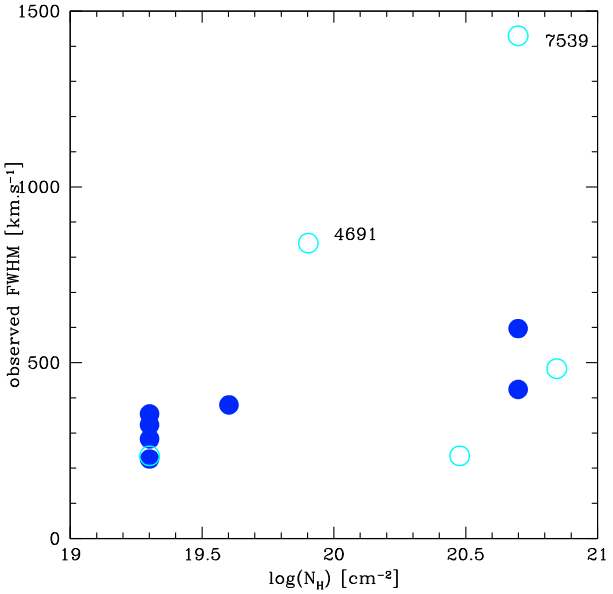

Fig. 13. Observed Lyα *FWHM* versus neutral column density showing a tentative correlation between the observed Lyα *FWHM* and the H I column density in the shell, for the FDF objects. The filled circles are objects with asymmetric Lyα profiles, the open circles are the others. The objects with double-peaked profiles, FDF 4691 and FDF 7539, are clearly distinct, showing the highest *FWHM*.

peaks) is predicted by theory, arising from Lyα resonant scattering through static H I media (Neufeld 1990), but surprisingly, observed double-peaked profiles are in general not interpreted as a signature of Lyα radiation transfer through static media (Fosbury et al. 2003; Christensen et al. 2004; Wilman et al. 2005; Venemans et al. 2005; Vanzella et al. 2008), even if they appear much less common than the asymmetric emission observed in all high-z LAEs. In the static case the separation of the peaks $\Delta\lambda$ is not only related to the thermal velocity of the H I gas, but depends also on the H I column towards the Lyα source, $N_{\rm HI}$. For a homogeneous slab one has:

$$\Delta\lambda^{\rm rest} = 2\lambda_0(-x_{\rm p}b/c) = 2.49\times10^{-7}\left(\frac{b}{12.85\,{\rm km\,s^{-1}}}\right)^{1/3}\left(\frac{N_{\rm HI}}{\rm cm^{-2}}\right)^{1/3}\ {\rm Å} \quad (2)$$

where c is the light speed, λ_0 is the restframe wavelength of Lyα, $b = \sqrt{V_{\rm th}^2 + V_{\rm turb}^2}$ is the Doppler parameter, and $x_{\rm p} = 0.88(a\tau_0)^{1/3}$ is the location of the peaks in units of the Doppler width (Neufeld 1990; Dijkstra et al. 2006b). For example, for $b = 12.85$ km s^{-1} and $N_{\rm HI} = 6.4\times10^{19}$ cm^{-2} one obtains $\Delta\lambda^{\rm rest} \sim 1$ Å. If applied to the $z \sim 3.65$ double peaked Lyα object of Vanzella et al. (2008), the observed velocity shift of 13 Å would indicate $N_{\rm HI} \sim 1.4\times10^{21}$ cm^{-2} for $b = 12.85$ km s^{-1}. Establishing accurate enough galaxy redshifts for these objects is important to determine wether it is a nearly static case (in which case zero velocity is between the two Lyα peaks), outflows (with both Lyα peaks redshifted), or other situations.

4.6. Observed Lyα *FWHM*

A possible correlation may be found between the observed *FWHM* and the neutral column density of the expanding shell, as shown in Fig. 13. If real, it may be used to estimate the H I column density in starbursts from a simple measurement of *FWHM*(Lyα). Such a correlation can easily be explained by radiation transfer effects: the Lyα optical depth increases with $N_{\rm HI}$ so that Lyα photons have to diffuse further in the wings to be able to escape the medium, which broadens the Lyα red wing.

All observed Lyα profiles are fitted with an intrinsic *FWHM* of ∼100 km s^{-1}, except for 4691, for which we have to start with an already very extended intrinsic Lyα line to reproduce the very broad double-peaked profile. Otherwise, more exotic scenarios, like a shell with a hole, have to be invoked.

The two correlations presented above ($FWHM_{\rm obs}$ vs. $N_{\rm HI}$ and $EW_{\rm obs}$ vs. $N_{\rm HI}$, Figs. 11 and 13) explain the observed anti-correlation shown by T07 between $FWHM_{\rm obs}$ and $EW_{\rm obs}$. Indeed, they are both related to the neutral column density $N_{\rm HI}$ which surrounds the starburst. The $EW_{\rm obs}$ increases with decreasing $N_{\rm HI}$ and the $FWHM_{\rm obs}$ increases with increasing $N_{\rm HI}$. Therefore, we should not observe objects with a large $EW_{\rm obs}$ and very broad lines, which is also confirmed by the observed $FWHM_{\rm obs}$ of LAEs which are always below 500 km s^{-1} (Rhoads et al. 2003; Dawson et al. 2004; Venemans et al. 2004). If the tentative correlation between $FWHM_{\rm obs}$ and $N_{\rm HI}$ truly holds, this would imply a maximum column density of $N_{\rm HI} \lesssim (2\text{–}4)\times10^{20}$ cm^{-2} in LAEs.

4.7. Escape fraction

The Lyα line escape fractions derived for our FDF objects range from 100% for the dust-free object FDF4691 to ∼2% for objects with the highest extinction. From our modeling we find that the main parameter determining the escape fraction is the dust amount in the shell. Furthermore, from all our modeling results already discussed above, it is clear that no single value of the Lyα escape fraction is expected for LBGs and LAEs, in contrast to the simplifying assumptions made in some models (e.g. Le Delliou et al. 2006).

Our model grids predict the following behaviour for the escape fraction:

- $f_{\rm e}$ increases with increasing $V_{\rm exp}$, because the Lyα optical depth decreases in a fast moving medium compared to the static case. Therefore the mean path of Lyα photons in the medium decreases, as does their chance of being absorbed by dust.
- $f_{\rm e}$ decreases with increasing $N_{\rm HI}$, because the Lyα optical depth is proportional to $N_{\rm HI}$.
- $f_{\rm e}$ decreases with increasing $E(B-V)$, obviously since with a larger number of absorbers in the medium, Lyα photons increase their chance of interacting with them.

However, the only clear correlation we found in the data between $f_{\rm e}$ and other parameters is with $E(B-V)$ (see Fig. 14). No correlation is found in particular with $V_{\rm exp}$ (our objects probably cover too small a range in velocity), and with $N_{\rm HI}$ (the variation in the dust-to-gas ratio is likely more dominant). In Fig. 14, we see also that, as expected, Lyα photons are more attenuated by dust than the continuum; indeed all LBG data points (circles) are located below the solid line corresponding to $f_{\rm e}({\rm cont}) = \exp(-\tau_{\rm a})$. The reason is that multiple resonant scattering of Lyα photons increases their path through the medium, and hence their chance of being absorbed by dust, compared to the continuum. Note that other dependences of $f_{\rm e}$ on $E(B-V)$ could be expected with other geometries. For example in clumpy media, the reflection of Lyα on the clump surfaces could ease the Lyα transmission for the same amount of dust (Neufeld 1991; Hansen & Oh 2006).

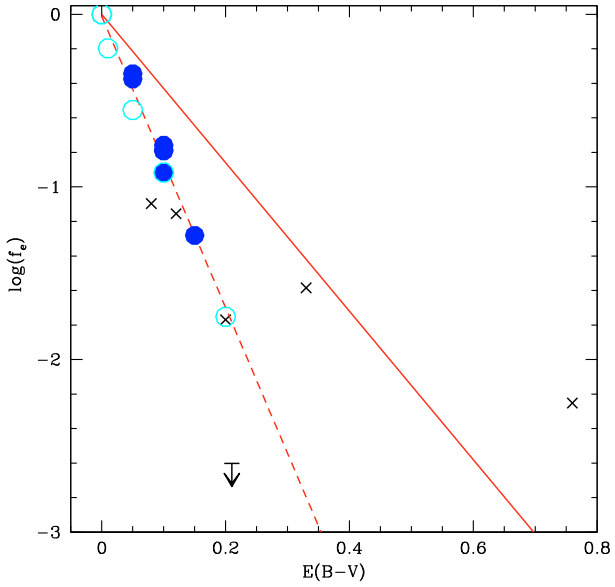

Fig. 14. Lyα escape fraction versus dust extinction in the gas for the LBG (circles) and local starbursts (crosses). We find a clear correlation between the Lyα escape fraction and the dust amount in the shell, for the 11 objects from the FDF. The filled circles stand for objects with asymmetric profiles, open circles the remaining ones. The solid line represents the continuum attenuation, $f_{e_{cont}} = \exp(-\tau_a) \approx \exp(-10 \times E(B-V))$, the dashed line the fit proposed in Eq. (3). The crosses and the upper limit are the integrated escape fractions from a sample of 6 local starbursts from Atek et al. (2008) plotted as a function of $E(B-V)$ measured from the Balmer decrement.

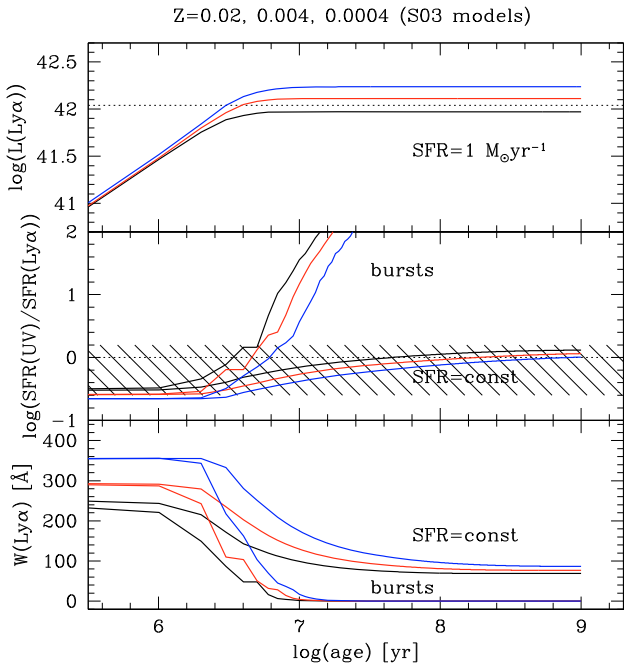

Fig. 15. Temporal evolution of Lyα and UV SFR predictions from the synthesis models of S03 for three metallicities ($Z = 0.02 = Z_\odot$ in black, 0.004 in red, and 0.0004 in blue) computed for instantaneous bursts and/or constant SF. *Top*: Lyα line luminosity in erg s^{-1} emitted per unit SF rate, assuming a Salpeter IMF from 0.1 to 100 $M_\odot$. The dotted line shows the "canonical" value based on Kennicutt (1998) and a standard Lyα/Hα ratio. *Middle*: logarithm of the UV to Lyα SFR ratio. The shaded area shows the allowed range for constant SF models with metallicities between 1/50 $Z_\odot$ and solar. *Bottom*: Lyα equivalent width.

We propose a fit to predict the escape fraction of Lyα photons knowing the dust extinction (dashed curve on Fig. 14):

$$f_e = 10^{-7.71 \times E(B-V)}. \quad (3)$$

Note that $E(B-V)$ in the formula is the extinction in the gas, which may be different from the extinction of the stars (Calzetti et al. 2000), as already mentioned above. Interestingly, the two static objects are also fitted by this formula, which illustrates that dust is really the dominant parameter governing the Lyα escape in our objects. One of these (4691) is dust-free, so its escape fraction is ∼1, but in the other object (7539), 30% of the Lyα photons escape the medium. For the same extinction, moving media present an escape fraction of 40−45%, which is consistent with the theoretical prediction that f_e increases with V_{exp}.

Empirical Lyα escape fractions have recently been measured by Atek et al. (2008) from imaging for a sample of 6 local starbursts. Their values are compared to our data for LBGs in Fig. 14. For $E(B-V) \leq 0.2$, our results are in good agreement with three local objects. SBS 0335-052 with an integrated extinction of $E(B-V)^{gas} \approx 0.21$ shows no Lyα emission, it is a net absorber. For larger $E(B-V)$ values, the Lyα escape fraction of two local starbursts (Haro 11 and NGC 6090) are higher than f_e predicted by our fit to the LBGs studied here. Deviations from a simple homogeneous shell geometry are the most likely explanation for this difference. This will be testable through detailed modeling both of the spatially resolved and integrated properties of the local objects.

Since the Lyα line flux is more strongly reduced (due to multiple scattering effects) than the adjacent continuum, the Lyα equivalent width depends on the extinction. This phenomenon is added to the one already known to result from the extinction difference between the gas and the stellar continuum. In principle, a measurement of $EW(\mathrm{Ly}\alpha)_{obs}$ could thus be used to determine the extinction, provided the intrinsic equivalent width EW_{int} is known. Concretely, the fit-relation between f_e and $E(B-V)^{gas}$ proposed above (Eq. (3)) translates into the following behaviour of Lyα equivalent width with extinction:

$$\log\left(\frac{EW_{obs}^{rest}}{EW_{int}}\right) = -E(B-V)^{gas}\,(7.71 - 0.4 k_\lambda\, r)$$
$$\approx -5.6\; E(B-V)^{gas} \quad (4)$$

where $k_{\lambda=1216\,\text{Å}} \approx 12$ and $r = E(B-V)^\star / E(B-V)^{gas} = 0.44$ according to Calzetti (2001). Adopting reasonable values for EW_{int} (e.g. from Fig. 15), this formula may be used to obtain a crude estimate of the extinction in LAEs based on a pure equivalent width measurement. An extinction corrected $SFR(\mathrm{Ly}\alpha)$ value can then be obtained from the Lyα luminosity using an appropriate SFR calibration from Fig. 15, consistently with the assumed value of EW_{int}.

4.8. SFR indicators

Given our quantitative analysis of Lyα radiation transfer, the determination of the Lyα escape fraction and of the extinction, we are now able to examine to what extent Lyα and the UV continuum provide consistent measures of the star formation rate. The main results of this exercise are shown in Fig. 16

First we note that three of our objects (1267, 4454, 5812) show observed, i.e. uncorrected SFR values corresponding to $SFR(\mathrm{Ly}\alpha) > SFR(\mathrm{UV})$. Such a result need not be inconsistent; this behaviour is indeed expected for young bursts or objects where constant star formation has not yet proceeded over long enough timescales, i.e. for timescales ≲10−100 Myr

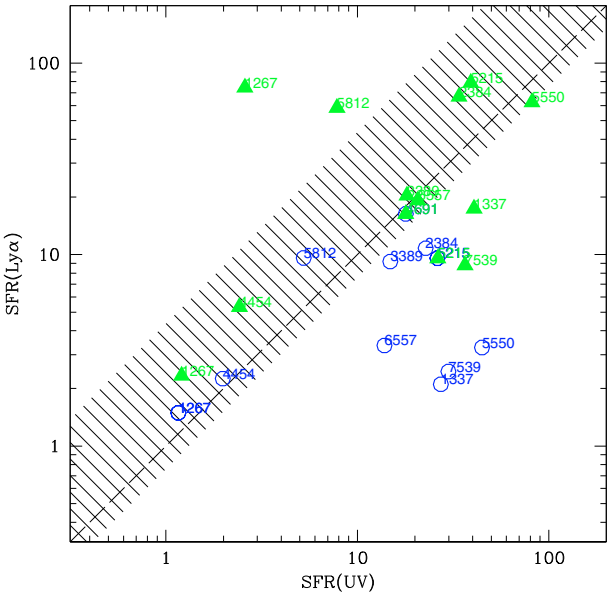

Fig. 16. Comparison of the SFR values determined from the UV continuum and from Lyα for our objects. Blue circles indicated the "observed", uncorrected SFR values from Table 1. Green symbols show the "true" values corrected for dust and transfer effects according to Eqs. (5) and (6). The shaded area shows the range allowed by synthesis models for the combination of the "true" $SFR(\mathrm{Ly}\alpha)$ and $SFR(\mathrm{UV})$ values taking age effects of constant SF models into account and allowing for metallicities between 1/50 $Z_\odot$ and solar (cf. Fig. 15). The dashed line indicates the one-to-one relation.

as shown in Fig. 15. In this case values up to $SFR(\mathrm{Ly}\alpha) \sim 4 \times SFR(\mathrm{UV})$ can be obtained; this allowed range of values for $SFR(\mathrm{Ly}\alpha)/SFR(\mathrm{UV})$ for constant SF is shown by the shaded region in Fig. 16. Indeed these objects also show among the largest $EW(\mathrm{Ly}\alpha)_{\mathrm{obs}}$, as expected from Fig. 15 for relatively young, but on average constantly star-forming, objects. Second, 4691 shows $SFR(\mathrm{Ly}\alpha) \approx SFR(\mathrm{UV})$ (observed), indicative of little or no dust, and confirmed by our modeling. Finally the remaining 7 objects show $SFR(\mathrm{UV}) > SFR(\mathrm{Ly}\alpha)$ with UV star formation rates up to ∼14 times larger than Lyα, a result found for the majority of LBGs and LAEs (e.g. Yamada et al. 2005; Gronwall et al. 2007).

We now correct these SFR indicators for the effects of dust and radiation transfer. One has

$$SFR(\mathrm{Ly}\alpha)^{\mathrm{true}} = SFR(\mathrm{Ly}\alpha)/f_{\mathrm{e}}, \quad (5)$$

with the Lyα escape fraction f_{e}. The UV SFR is corrected assuming the Calzetti law and the extinction $E(B-V)$ derived from the Lyα line fit, i.e.

$$SFR(\mathrm{UV})^{\mathrm{true}} = SFR(\mathrm{UV}) \times 10^{+0.4E(B-V)^\star k_{\mathrm{UV}}}, \quad (6)$$

with $E(B-V)^\star = 0.44E(B-V)$. For our objects $k_{\mathrm{UV}} = k_{1600} \approx 10$ is appropriate. Using $E(B-V)$ derived from our Lyα fits, the resulting "true" SFR values for all our objects are plotted in Fig. 16 (green triangles). For the majority of the objects we find that their corrected SFR values show much less dispersion between Lyα and UV based measurements than observed, uncorrected values. Three objects (1337, 5215, 7539) seem to require even lower Lyα escape fractions (i.e. larger extinction) to reduce the differences between their SFR indicators further. Adopting Eq. (3) and imposing $SFR(\mathrm{Ly}\alpha) = SFR(\mathrm{UV})$ would imply an extinction $E(B-V)$ of (0.19, 0.07, 0.18) compared to our estimate of (0.1, 0.1, 0.05) mag from line fitting. Similarly the extinction seems to be overestimated in FDF 5812 and for the high N_{HI} solution of 1267. The maximum extinction allowed to obtain SFR consistencies for these objects within the shaded region is $E(B-V) = 0.09$ and 0.06 for 1267 and 5812 respectively. Most of these "adjustments" are within a factor of 2 uncertainty. We therefore conclude that the results based on our Lyα line fits using radiation transfer models improve the consistency between UV continuum and Lyα line based SFR indicators.

4.9. Other correlations

Several correlations have been found between Lyα and other properties of LBGs from the analysis of large spectroscopic samples. When grouping their ∼1000 LBG spectra according to Lyα equivalent width, Shapley et al. (2003) found the following main correlations with decreasing $EW(\mathrm{Ly}\alpha)_{\mathrm{obs}}$ (i.e. from emission to absorption): *1)* The extinction increases; *2)* the strength of the low-ionisation interstellar lines increases; *3)* the velocity shift between these interstellar lines and the Lyα peak, $\Delta v(\mathrm{em}-\mathrm{abs})$, increases; and *4)* the dust-corrected SFR increases. Correlations 1, 2, and 4 have also been found in other samples (e.g. Noll et al. 2004; Tapken et al. 2007). We now examine whether these correlations also hold for our small sample, and how well our model explains them.

4.9.1. $E(B-V)$ versus Lyα EW

A decrease of $EW(\mathrm{Ly}\alpha)_{\mathrm{obs}}$ with increasing extinction is expected from our radiation transfer models, e.g. when the intrinsic equivalent width is constant (see Eq. (4)). This seems the simplest explanation for the trend observed between the average LBG spectra, also given the relatively long SF timescales generally observed in LBGs, which implies a fairly constant intrinsic $EW(\mathrm{Ly}\alpha)_{\mathrm{int}}$.

The 11 individual LBGs analysed here show no clear trend between $EW(\mathrm{Ly}\alpha)_{\mathrm{obs}}$ and $E(B-V)$. Given the relatively large scatter in the derived gas-to-dust ratio (see Fig. 10), it appears that the clearest observational trend found is instead between EW_{obs} and N_{HI} (Fig. 11). If on average the gas-to-dust ratio is constant, any correlation between EW_{obs} and N_{HI} would imply a correlation between $E(B-V)$ and $EW(\mathrm{Ly}\alpha)_{\mathrm{obs}}$, as observed by Shapley et al. (2003).

4.9.2. EW(LIS) versus $EW(\mathrm{Ly}\alpha)$

Our model does not make direct predictions of the strengths of interstellar absorption lines. For this reason and since most of the observed low ionisation interstellar lines are saturated (Shapley et al. 2003) we are not able to quantitatively examine this correlation.

Ferrara & Ricotti (2006) propose to explain the behaviour of EW(LIS) by cold debris whose covering factor decreases as a function of time in a dynamical outflow model. EW(LIS) is then mostly related to the wind velocity (constrained by $\Delta v(\mathrm{em}-\mathrm{abs})$) which according to these authors may vary with $EW(\mathrm{Ly}\alpha)_{\mathrm{obs}}$. Verifying observationally whether and how wind velocity varies and quantifying the covering factor of the cold outflowing gas is therefore important to test this scenario.

4.9.3. Δv(em – abs) versus $EW(\mathrm{Ly}\alpha)$

Shapley et al. (2003) measure velocity shifts between 475 ± 25 and 795 ± 3 km s^{-1} for their four groups (quartiles) of LBGs with decreasing $EW(\mathrm{Ly}\alpha)_{\mathrm{obs}}$. To verify this trend we have

remeasured Δv(em − abs) and other quantities from the composite spectra of Shapley et al. (2003); overall our measurements are within 1σ, except for group 1 (with the strongest Lyα absorption) where we obtain Δv(em − abs) = 703 km s^{-1}. The uncertainty cited for this group thus appears to be underestimated. Does this observed trend imply a systematic variation of the average outflow velocity between the spectral groups? For example, if true, this could imply an increase of the average wind velocity from $V_{\rm exp} \approx 1/3 \times \Delta v$(em − abs) $\sim$ 160 to 235 km s^{-1} (or to 265 km s^{-1} using Shapley's value for group 1) if spherical shell models apply, as argued earlier.

As already mentioned above, the expansion velocities derived for our objects and those measured for 2 of them as well as the typical reddening values are in good agreement with the data of Shapley et al. (2003). However, within our small sample we do not find any systematic variation of $V_{\rm exp}$, and clearly the reddening variations we find are large compared to the difference of the mean extinction between groups 3 and 4 of Shapley (where our objects would lie) and compared to the dispersion of $E(B-V)$ within these groups.

Shapley stresses that "none of the correlations with Δv(em − abs) is as significant as the trends among EW(Lyα)$_{\rm obs}$, EW(LIS), and $E(B-V)$". For example, when grouped according to Δv(em − abs), the objects of Shapley et al. (2003) show several trends opposite to those trends found between the groups constructed according to EW(Lyα)$_{\rm obs}$[3]. The reality and significance of this behaviour is thus questionable. In fact we find two effects, a radiation transfer and an "instrumental" one, which could artificially lead to such a behaviour.

First, while for expanding shells with column densities $N_{\rm HI} \gtrsim 10^{20}$ cm^{-2} the main peak of the Lyα profiles is indeed redshifted by twice the expansion velocity (as pointed out by Verhamme et al. 2006), the peak emerges at lower velocities ($\sim 1 \times V_{\rm exp}$) for lower column densities. This transition is clearly illustrated in Fig. 17. If Shapley's spectral groups correspond on average to a sequence with increasing $N_{\rm HI}$ (from Lyα in emission to absorption) and if this transition happens somewhere within this sample, it would mean that the real spread of outflow velocities would be considerably reduced from ~238 to 265 km s^{-1} (or 235 with our measurement for group 1).

A second, unavoidable effect also alters the observed velocity shift between Lyα and the interstellar lines. Indeed, given the increasing strength of broad Lyα absorption in groups 2 and 1 compared to the other groups, the relatively low spectral resolution of the composite spectra affects the measurement of the Lyα line fit, introducing a systematic shift. For illustration we show in Fig. 18 the high-resolution spectrum of cB58 – an LBG with Lyα properties characteristic of group 1 – and the effect lower spectral resolution has on the measurement of the Lyα peak. Interestingly (cf. Mas-Hesse et al. 2003), a limited spectral resolution, such as the one of ~400−700 km s^{-1} of the composite spectra of Shapley et al. (2003), can lead to an overestimate of the true Lyα line redshift in objects with a steeply rising "underlying" spectrum. In other words, due to the appearance of the broad Lyα absorption wing, the measurement of Δv(em−abs) may be affected by a systematic shift that increases with decreasing EW(Lyα)$_{\rm obs}$ i.e. towards the group 1 with the strongest Lyα absorption. As the exercise in Fig. 18 shows, this shift can be of the same order as the apparent velocity differences between different LBG subgroups. Thus we conclude that the observed

[3] E.g. Instead of decreasing, $E(B-V)$ increases with increasing EW(Lyα)$_{\rm obs}$ between LBGs grouped according to Δv(em − abs) (cf. Figs. 3 and 16 of Shapley et al. 2003).

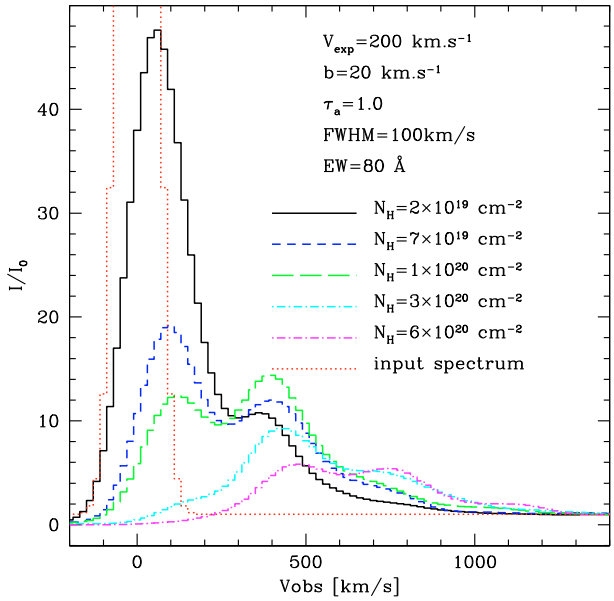

Fig. 17. Dependence of the Lyα line profile on $N_{\rm HI}$ for typical shell parameters. Note the clear shift of the peak of the emission profile from low velocity ($\sim$100 km s^{-1} $\approx 0.5 \times V_{\rm exp}$) to twice the shell velocity with increasing $N_{\rm HI}$, typical for $N_{\rm HI} \gtrsim 10^{20}$ cm^{-2}.

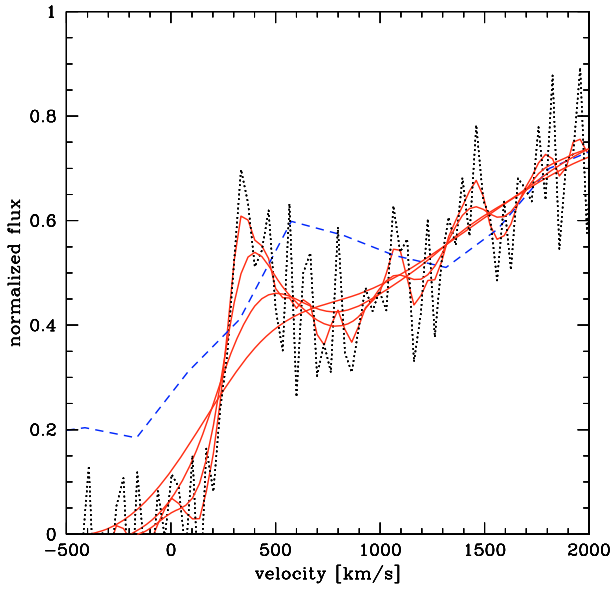

Fig. 18. Effect of spectral resolution on the Lyα line shift measurement. The dotted line is the observed spectrum of cB58 from Pettini et al. (2002) with a resolution of 58 km s^{-1}. Red solid lines show the same spectrum convolved to resolutions of 100, 200, 400, and 700 km s^{-1}. The blue dashed line is the spectrum of the first group of Shapley et al. (2003) normalised to the one of cB58 at +1700 km s^{-1}. Note the progressive redshift of the Lyα peak (observed at +355 km s^{-1} in the original cB58 spectrum) by up to ~200 km s^{-1} for a resolution of 400 km s^{-1}, typical of the composite spectra of Shapley et al. (2003).

variations between Lyα and the IS lines found between the subgroups of Shapley et al. (2003) and possible correlations with other quantities cannot reflect the simple behaviour of the real outflow velocity. More work is needed to clarify the possible link between outflow velocities and other properties of LBGs.

Our radiation transfer calculations show that the variations of $V_{\rm exp}$ found between the objects fitted here have a relatively minor influence on properties such as EW(Lyα), the Lyα escape

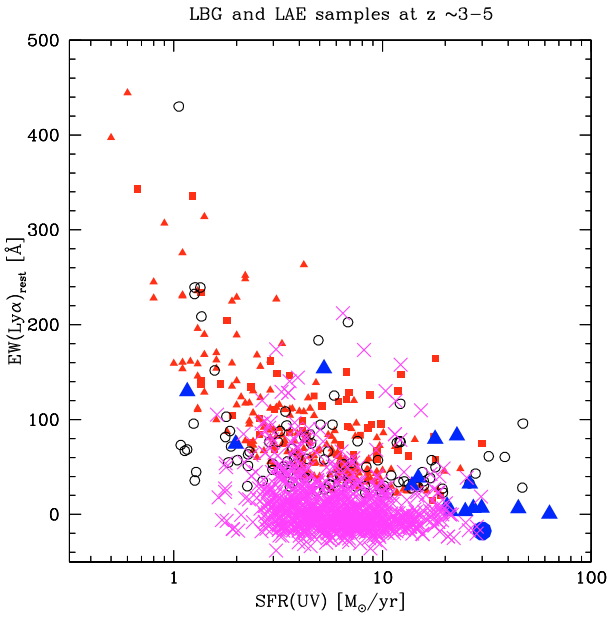

Fig. 19. Observed restframe Lyα equivalent width of LBGs and LAEs as a function of their UV star formation rate (uncorrected for reddening). The following data is shown: LBGs from Tapken et al. (2007) (blue triangles), cB58 Pettini et al. (2002) (blue circle), and the individual objects from Shapley et al. (2003) (magenta crosses). LAEs or LAE-candidates from Yamada et al. (2005) (red triangles) Ouchi et al. (2007) (red squares) and from Gronwall et al. (2007) (black circles). The data clearly shows the absence of high equivalent width objects at high SFR, which we explain as being due to dust/radiation transfer effects. For further details see text.

fraction etc. It appears that as long as global outflows with velocities of several 100 km s^{-1} are present, other parameters are more dominant.

4.9.4. SFR(UV) versus *EW*(Lyα)

Trends or correlations between $EW(\mathrm{Ly}\alpha)_{\mathrm{obs}}$ and the star formation rate have been noted by many groups and are found not only for LBGs, but also for LAEs (e.g. Shapley et al. 2003; Ando et al. 2004; Tapken et al. 2007). A compilation of available data is shown in Fig. 19, where we include the following data : LBGs from Tapken et al. (2007), cB58 Pettini et al. (2002) (blue symbols), and the individual objects from Shapley et al. (2003) (magenta crosses); LAEs or LAE-candidates from Yamada et al. (2005); Ouchi et al. (2007) (red symbols) and from Gronwall et al. (2007) (black circles). Note that Tapken's LBGs include four $z \sim 4.5$–5 objects, Yamada's sample of 198 LAEs spans $z \sim 3.3$ to 4.8, Ouchi's 84 spectroscopically confirmed LAEs have $z \sim 3.1$, 3.7 and 5.7. All other objects have redshifts have $z \sim 2.7$–3.2. Note that none of the data was corrected for reddening. *SFR*(UV) is therefore directly proportional to the observed UV magnitude of the objects.

The observations summarised in Fig. 19 show *1)* the absence of strong Lyα emitters (high EW_{obs}) at high *SFR*(UV); *2)* the existence of objects with $EW(\mathrm{Ly}\alpha)_{\mathrm{obs}} \gtrsim 100$ Å for low SFR; *3)* the possible existence of a maximum value of $EW_{\mathrm{max}}(\mathrm{Ly}\alpha)$ as a function of *SFR*(UV); and *4)* a wide range of $EW(\mathrm{Ly}\alpha)_{\mathrm{obs}}$ at low star formation rates ($SFR(\mathrm{UV}) \lesssim 10\ M_\odot\ \mathrm{yr}^{-1}$). Although the $z \sim 3$ samples span the largest range in *SFR*(UV) there does not seem to be a systematic trend with redshift. We therefore retain all objects, irrespective of their *qz*. We suggest the following explanations for the trends shown in Fig. 19.

1. The absence of high EW_{obs}-high SFR objects (1) is due to radiation transfer effects and the presence of dust, which unavoidably lead to a stronger reduction of Lyα photons compared to the adjacent continuum (cf. Sect. 4.7). The probability that high UV-SFR objects are powered by one or few instantaneous bursts is very small; hence their intrinsic Lyα equivalent widths must be close to that expected for constant SF, i.e. $EW(\mathrm{Ly}\alpha)_{\mathrm{obs}} > 70$–90 Å and up to ~250–360 Å depending on metallicity (cf. Fig. 15). Radiation transfer and the presence of dust reduce $EW(\mathrm{Ly}\alpha)_{\mathrm{obs}}$ from the intrinsic to the observed values;
2. strong Lyα emitters with $EW(\mathrm{Ly}\alpha)_{\mathrm{obs}} \gtrsim 100$ Å correspond to young ($\lesssim$50 Myr) objects, with the exact age limit depending on the detailed SF history. Equivalent widths up to ~360 Å can be explained by stellar populations with "normal" Salpeter-like IMFs and metallicities $Z \gtrsim 1/50\ Z_\odot$. The strong emitters probably show little or no reddening, which would otherwise rapidly reduce the observed equivalent width. Observationally most of these objects are found as LAEs; few LBGs show such strong emission (cf. Shapley et al. 2003);
3. the trend of $EW_{\mathrm{max}}(\mathrm{Ly}\alpha)$ ("upper envelope") as a function of *SFR*(UV) (i.e. UV magnitude) is most likely due to an increase of $E(B-V)$ with *SFR*(UV). An increasing dust optical depth will progressively reduce the intrinsic Lyα equivalent widths providing a natural continuity between the objects discussed in 2) and 1). Presumably the H I column density also increases with magnitude (i.e. UV SFR) maintaining a "reasonable" spread in the gas-to-dust ratio. Ultimately, the main underlying parameter governing the trends with UV magnitude may be the galaxy mass. We will discuss this further below;
4. the large spread in $EW(\mathrm{Ly}\alpha)_{\mathrm{obs}}$ at faint magnitudes ($SFR(\mathrm{UV}) \lesssim 5$–$10\ M_\odot\ \mathrm{yr}^{-1}$) results most likely from two effects: first the relatively small amount of dust, which does not eliminate the high EW_{obs} objects, and second the larger variety of SF histories/timescales – i.e. an enhanced role of "stochastic SF events" – made more plausible for objects of smaller absolute scale (mass or total SFR).

5. Other derived properties

In other contexts it may be of interest to derive properties such as the total neutral hydrogen mass in the outflow and the mass outflow rate. The following formulae can be used to estimate these quantities.

5.1. Neutral gas mass

The H I mass in the shell is related to its column density N_{HI} and radius r by

$$M_{\mathrm{HI}} \approx 10^7 \left(\frac{r}{1\ \mathrm{kpc}}\right)^2 \left(\frac{N_{\mathrm{HI}}}{10^{20}\ \mathrm{cm}^{-2}}\right) M_\odot. \quad (7)$$

Assuming $r = 1$ kpc, we find neutral gas masses of the order of $\sim 2\times10^6$ to $10^8\ M_\odot$, with a median of $7\times10^6\ M_\odot$. If the H I were found in shells with radii similar to the optical sizes measured from D_{25} for local starbursts, $r_{25} \sim 5$–50 kpc, these estimates have to be increased by a factor 25–2500. A plausible lower limit of $r > 1.6\,h^{-1}$ kpc is derived by Shapley et al. (2003) from

the typical half-light radius of LBGs; similarly the examination of close LBG pairs puts an upper limit of $r \lesssim 25\,h^{-1}$ proper kpc on the physical dimension of the gas giving rise to strong interstellar absorption lines (Adelberger et al. 2003).

5.2. Mass outflow rates

Following Pettini et al. (2000) the mass loss rate involved in the outflow may be estimated as:

$$\dot{M}_{\rm HI} = 6. \left(\frac{r}{1\ {\rm kpc}}\right)\left(\frac{N_{\rm HI}}{10^{20}\ {\rm cm}^{-2}}\right)\left(\frac{V_{\rm exp}}{200\ {\rm km\,s}^{-1}}\right) M_\odot\ {\rm yr}^{-1}, \quad (8)$$

Again assuming $r = 1$ kpc, we derive mass outflow rates between ~0.2 and 100 $M_\odot\ {\rm yr}^{-1}$. For larger radii $\dot{M}_{\rm HI}$ has to be increased accordingly. The estimated outflow rates are thus comparable to the star formation rate, as already found earlier (e.g. Pettini et al. 2000; Grimes et al. 2007). In cases with the lowest velocities (quasi-static shells, i.e. in 2−3 of our objects), there is most likely no true outflow out of the galaxy.

6. A unifying scenario for LBGs and LAE, and implications

In Paper II, based on our modeling results for cB58 and on empirical data, we have proposed a unifying scenario to explain Lyα emission and absorption and the observed trends in LBGs. We will now discuss this scenario in the light of the results from the FDF objects and of the discussion in the present paper, and we will show how this scenario should also apply to LAEs.

In Paper II we suggested that the bulk of the LBGs intrinsically have $EW({\rm Ly}\alpha)_{\rm int} \sim 60$−$80$ Å or larger, and that the main physical parameter responsible for the observed variety of Lyα strengths and profiles in LBGs are $N_{\rm HI}$ and the accompanying variation of the dust content. Here, we propose that the same also holds for most LAEs, and that the larger Lyα equivalent widths found in (some of) these objects are due to the younger ages of the SF population, independently of their SF histories. For example, $EW({\rm Ly}\alpha)_{\rm int}$ up to $\lesssim$300−400 Å can be expected at ages $\lesssim$50 Myr and for metallicities $\lesssim 1/5\ Z_\odot$ (cf. Fig. 15). Any differences between intrinsic and observed Lyα equivalent widths are then due to radiation transfer and dust effects.

In Paper II, we have shown that these effects transform, e.g. for an extinction of $E(B-V) \sim 0.3$ as found for cB58, a spectrum with an intrinsic Lyα emission with $EW({\rm Ly}\alpha)_{\rm int} \gtrsim 60$ Å into an absorption-dominated spectrum of LBGs. In the objects modeled here, Lyα is always found in emission, with observed $EW({\rm Ly}\alpha)_{\rm obs} \sim 6$−$150$ Å. Again, the intrinsic Lyα emission determined from our line fits is found to be stronger with $EW({\rm Ly}\alpha)_{\rm int} \sim 50$−$280$ Å. For all these LBG examples, covering the full range of Lyα line strengths observed by Shapley et al. (2003), the intrinsic Lyα properties are thus compatible with expectations of starbursts with constant star formation. For LAEs the same scenario can also hold, provided the extinction and/or H I column density are sufficiently low, and provided the age of the highest $EW({\rm Ly}\alpha)_{\rm obs}$ objects is relatively young.

We now discuss the arguments supporting a continuity and even a strong overlap between LBGs and LAE; subsequently we will summarise the main observational evidence supporting our scenario.

6.1. LBGs and LAE, overlapping population with a sequence driven mostly by mass?

We suggest the following overlap and distinctions between LBGs and LAEs at a given redshift:

1. LAEs brighter than a certain limiting magnitude, $M_{\rm lim}$, in the continuum are the same population as LBGs with strong Lyα emission (i.e. $>EW^{\rm rest}_{\rm lim}$);
2. at magnitudes fainter than $M_{\rm lim}$, LAEs represent less massive objects than LBGs;
3. the remaining LBGs, i.e. those with $EW({\rm Ly}\alpha) < EW^{\rm rest}_{\rm lim}$ and Lyα in absorption and hence not selected as LAEs, can cover a wide range of galaxy masses, SFR, and SF histories.

At redshift $z \sim 3$ the overlap between LAEs and LBGs corresponds to approximately ~25% of the LBG population, and ~23% of the LAE population, as we will discuss below. The amount of overlap, hence the value of $M_{\rm lim}$ likely varies with redshift. Let us now justify these statements in more detail.

That there should be a continuity between LBGs and LAEs and a strong overlap between the different populations seems quite obvious as their distinction stems from a "UV-continuum" versus "emission line" selection, based, however, on the same spectral range (restframe UV). Furthermore the Lyman break or drop-out criterion is also applied as a selection criterion for many LAE samples (e.g. Taniguchi et al. 2005; Ouchi et al. 2007), and in any case LAEs are expected to show a Lyman break, even if too faint to be measured from the current data. A continuity between LBGs and LAEs is also supported by the overlap of many of their observed properties, such as magnitudes, colors, and others (e.g. Gawiser et al. 2006; Gronwall et al. 2007; Ouchi et al. 2007; Nilsson et al. 2007; Martin et al. 2008; Lai et al. 2008), in addition to the ones already discussed above (SFR(UV), SFR(Lyα), Lyα equivalent widths). Furthermore, the spatial distribution of LBGs and LAEs also show very similar correlation lengths, both at $z \sim 3$ and 4.5 where measurements are available (Adelberger et al. 2005; Gawiser et al. 2007; Kovač et al. 2007). Finally, at $z \sim 3$ the relative number densities of LAE/LBG can also be understood: in the magnitude range $R_{\rm AB} < 25.5$ covered both by the LBG sample of Shapley et al. (2003) and the LAE sample of Gronwall et al. (2007), one has a ratio of LAE/LBG ~1/3, according to the latter authors. This is identical to the fraction of ~25% of LBGs showing strong Lyα, $EW({\rm Ly}\alpha)_{\rm obs} \sim 20$ Å, since this limit is the same as the selection limit of the Gronwal sample[4]. Adopting the same magnitude limit ($R < 25.5$) for both samples, we find no significant difference between the equivalent width distributions of the $z \sim 3$ LBG and LAE sample, as shown in Fig. 20. Indeed, while the $EW_{\rm obs}$ distribution of Shapley's total LBG sample differs from that of Gronwal, the probability that both distributions are drawn from the same parent distribution is 92 % (according to the 2 sided Kolmogorov-Smirnov test), once this same magnitude limit is applied to both samples. This overlap with the LBGs concerns 37 out of 160 LAEs (23%) from Gronwal's statistically complete LAE sample at $z \sim 3.1$.

We therefore conclude that LAEs above a certain magnitude limit represent the same population as LBGs with Lyα emission (point 1 above); furthermore the LAE selection method allows one to find strong emission line objects drawn from a larger

[4] Applying the criteria $R_{\rm AB} < 25.5$ and $EW({\rm Ly}\alpha)^{\rm rest}_{\rm obs} > 20$ Å to Shapley's data we find 175 out of 814 LBG, i.e. 21.5%. Dropping the restriction on R we obtain 22.5 %, similar to the ~25% of Shapley et al. (2003).

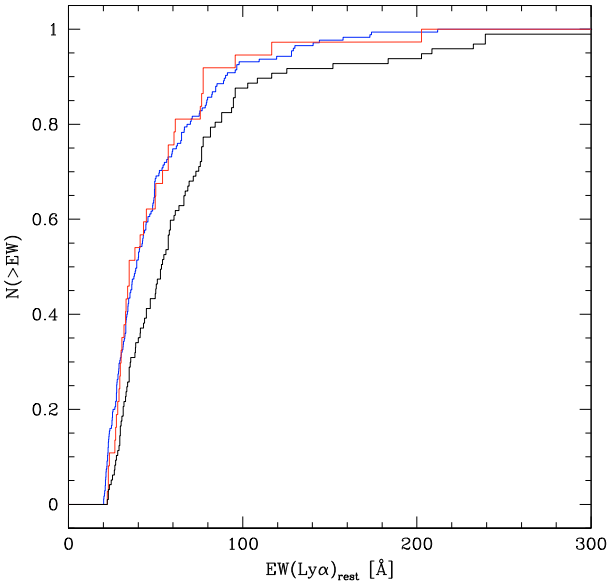

Fig. 20. Cumulative distribution of the observed Lyα equivalent widths of $z \sim 3$ samples of LAEs and LBGs: Shapley's LBGs with $R < 25.5$ and $EW(\mathrm{Ly}\alpha)^{\mathrm{rest}}_{\mathrm{obs}} > 20$ Å in blue, LAEs from Gronwall et al. (2007) fulfilling the same condition in red, and full LAE sample of Gronwal et al. in black. The probability that the blue and red distributions are drawn from the same parent distribution is 92%, according to the 2 sided Kolmogorov-Smirnov test.

range of continuum brightness than the LBG selection, as also shown in Fig. 19 (point 2). The "remaining" LBGs, corresponding to three quartiles of Shapley, cannot be found through the LAE selection technique, and represent thus a separate class of star forming objects. As many LBG studies have shown, their parameters (mass, SFR etc.) cover a wide range (point 3).

If a continuity and overlap exists between LBGs and LAEs, what then is the main parameter(s) "driving" the observed Lyα strength? From the Lyα radiation transfer in expanding shells we have seen that the extinction (described here by $E(B-V)$ or the dust optical depth) plays a role in determining the strength of Lyα[5]. The next important parameter N_{HI}, and the resulting variation in dust/gas ratio, as well as possibly deviations from the simple geometry considered here, likely introduce the required scatter around an oversimplified 1-dimensional scaling. Instead of the extinction, other parameters, such as the stellar mass $M_\star$ of the galaxy, its SFR, or others may be physically more fundamental, as suggested in Paper II. In this case LBGs and LAEs at the same redshift would represent a continuity with decreasing mass, at least on average, and correlations between $M_\star$, $E(B-V)$, and N_{HI} would explain the observed trends, including those of Lyα.

Among LBG samples, Pentericci et al. (2007) have found that LBGs at $z \sim 4$ with Lyα emission are less massive on average than LBGs with Lyα in absorption. The same trend has also been found by Erb et al. (2006) for $z \sim 2$ LBGs. Comparing LBGs and LAE, it is well established that LAEs show lower UV (i.e. continuum-based) star formation rates, and tend to have lower stellar masses than LBGs at similar redshift (cf. Reddy et al. 2006; Pirzkal et al. 2007; Gronwall et al. 2007; Gawiser et al. 2007; Overzier et al. 2008; Lai et al. 2008). The measured correlation length and galaxy bias of LBGs and LAEs are also consistent with a lower mass for the ensemble of LAEs, as discussed recently by Gawiser et al. (2007). At $z \sim 1-2$ clear correlations between the total SFR and stellar mass $M_\star$ are found for UV star formation rates covering a similar range as those observed in $z \sim 3$ LAEs and LBGs (Elbaz et al. 2007; Daddi et al. 2007; Noeske et al. 2007). Furthermore we know that extinction scales with the total (IR plus UV) SFR (e.g. at $z \sim 2$ see Reddy et al. 2006). Except for the behaviour of the H I column density with galaxy mass, which is so far unknown, all quantities thus show the required trend consistent with our scenario.

6.2. LBGs and LAEs: age and SF history differences?

As already pointed out in Paper II, stellar population studies of LBGs consistently find ages of several tens to hundreds of Myr and favour constant star formation over this timescale (see e.g. Ellingson et al. 1996; Pettini et al. 2000; de Mello et al. 2000; Papovich et al. 2001; Shapley et al. 2001). In this case an intrinsic $EW(\mathrm{Ly}\alpha)_{\mathrm{int}}$ of ~60–100 Å is unavoidable (cf. Fig. 15). Although fewer studies have been undertaken on the stellar populations of LAEs, it appears that some of them are younger than LBGs. For example, using the sample of $z = 3.1$ LAEs from Gronwall et al. (2007), Gawiser et al. (2007); Lai et al. (2008) find a large spread of ages (from ~20 Myr to ~1.6 Gyr) and a decrease of the mean age with decreasing mass and near-IR luminosity. Similarly, young ages (and low masses) have been found from studies of LAEs at higher redshift (e.g. Pirzkal et al. 2006; Finkelstein et al. 2007b).

No age constraint can be derived from Lyα alone for objects with $EW(\mathrm{Ly}\alpha)_{\mathrm{obs}} \lesssim 100$ Å, as such equivalent widths can be obtained for constant SF and taking into account various degrees of Lyα suppression by dust. On the other hand, $EW(\mathrm{Ly}\alpha)_{\mathrm{obs}} > 100$ Å requires ages of $\lesssim$10–50 Myr at maximum, depending on the exact SF history (Fig. 15); furthermore in such cases the amount of dust must be relatively low (e.g. $E(B-V) \lesssim 0.05$–0.1 for $EW^{\mathrm{rest}}_{\mathrm{obs}}/EW_{\mathrm{int}} = 0.5$ and $r = 0.44$–1, according to Eq. (4)) to maintain a high Lyα equivalent width. In other words, for the vast majority of the LBGs, Lyα provides no age constraint, whereas LAEs with $EW(\mathrm{Ly}\alpha)_{\mathrm{obs}} \gtrsim 100$ should have ages of $\lesssim$10–50 Myr. These simple predictions appear in good agreement with the age estimates of LBGs and LAEs discussed above.

What can be inferred about the SF timescale/duration in LBGs and LAEs and possible differences between the two classes? As already mentioned, for the LBGs modeled in detail here and in Paper II, our Lyα modeling results require relatively high intrinsic Lyα equivalent widths, corresponding to constant star formation over timescales $\gtrsim$20–50 Myr or longer; Lyα alone does not allow us to determine an upper limit for the duration of SF. For LAEs with high equivalent widths ($\gtrsim$100 Å) there is a degeneracy between age and SF duration, but long SF timescales are not excluded from their Lyα properties. Even less strong LAEs could be explained with constant SF (and hence unconstrained SF duration). For example objects with $EW(\mathrm{Ly}\alpha)_{\mathrm{obs}} = 20$ Å – a value close to the detection criterion commonly adopted – could be explained with a small amount of extinction, $E(B-V)^{\mathrm{gas}} \sim 0.1$, for an intrinsic equivalent width three times larger, according to Eq. (4). From Lyα alone, relatively long SF timescales could thus be possible both for the LBGs studied here and for the typical LAEs. However, more "bursty", intermittent SF histories may be more plausible for lower mass objects, such as LAEs. The suggestion of relatively long timescales for LAEs is e.g. compatible with the ages

[5] $E(B-V)$ is proportional to the dust absorption optical depth, which – associated with the effect of resonant scattering – determines the absorption probability of Lyα photons.

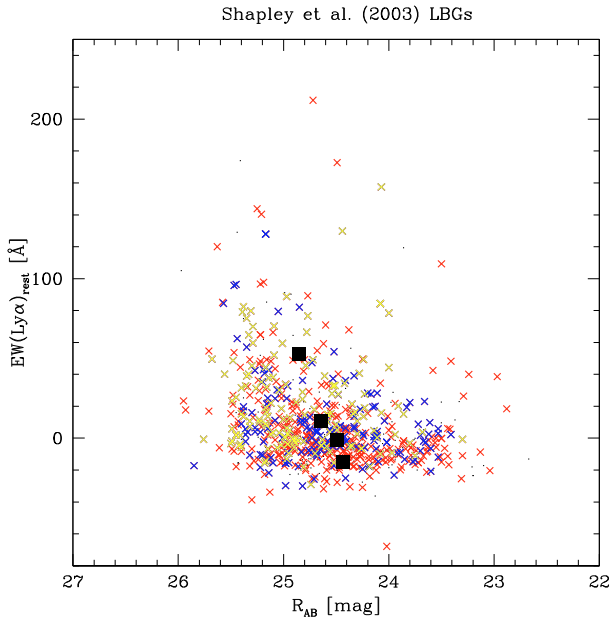

Fig. 21. Observed restframe Lyα equivalent width versus R_{AB} magnitude for the ∼800 LBGs of Shapley et al. (2003) (shown as crosses). The total EW_{obs} is plotted here, including both absorption and emission components if present. Colors indicate different amounts of extinction $E(B-V)$ estimated from the $G-R$ color as described in Shapley et al.: $E(B-V) > 0.2$ in black, red: 0.1−0.2, blue: 0.05−0.1, and yellow: $E(B-V) < 0.05$. The corresponding values of the four LBG groups of Shapley et al. are show as filled squares. Note the apparent existence of low $E(B-V)$, low $EW(\mathrm{Ly}\alpha)_{obs}$ objects, which could be dominated by stellar absorption.

of ∼160 Myr to 1.6 Gyr derived by Lai et al. (2008); however these age estimates probably provide upper limits, as derived assuming constant SF, and younger ages are also obtained when multiple components are allowed for.

Potentially the most interesting to constrain the SF timescale are objects with a low Lyα equivalent width (faint emission or even absorption) and low extinction. If the super-shell model applies to such objects and if their velocities are comparable to typical LBGs, observations of Lyα in absorption could indicate a post-starburst phase dominated by stellar absorption, as clear from Fig. 3 of Paper II. In fact, such objects seem to exist in the $z \sim 3$ LBG sample of Shapley et al. (2003), as shown Fig. 21. Finding objects with shorter SF timescales among the low SFR objects, which may also be seen in this figure, appears more plausible given the stronger dependence on "stochasticity" discussed earlier. However, whether these objects are truly short duty-cycle, post-starburst objects with little dust remains to be verified. Otherwise different geometries and kinematics may need to be invoked and the radiation transfer models reexamined for these objects. Observations of stellar UV features, such as C IV and Si IV and other H recombination lines (e.g. Hα) should in principle allow us to test this hypothesis and hence provide interesting constraints on the duty-cycle of these objects.

6.3. Open questions and further tests of the scenario

Although many arguments support our scenario described above, several important tests should be carried out. For example, a correlation between the galaxy mass and the H I column density remains to be established. Furthermore, does the dust mass increase with stellar mass? In other words, how does the dus-to-gas ratio evolve with galaxy mass? Also, how well do the proposed correlations hold for individual objects? And what governs the dispersion around such correlations?

Concerning LAEs, direct measurements of their ISM properties (velocity shifts, ISM covering factors etc.) would be very useful. Although it can be expected that these sources show outflows, as well established for the majority of LBGs, such observations remain to be performed. This could also be important to examine possible differences in the homogeneity and the covering factor of the ISM in these objects.

An unclear issue raised by our study concerns the fainter LBGs with low Lyα equivalent widths or Lyα in absorption. Are these, presumably less massive objects, sufficiently dust-rich to suppress Lyα emission, are they post starburst objects, or what other process(es) explain their absence of Lyα emission?

A larger number of deep high quality spectroscopic observations, multi-wavelength data, and accompanying modeling should help to answer these questions in the near future.

6.4. Implications

Our scenario proposed for LBGs and LAEs has several notable implications, most of them already mentioned in Paper II.

First, our analysis has clearly shown that LBGs exhibit quite significant variations in their Lyα escape fraction, as apparent also from earlier comparisons of Lyα and other SFR indicators. Such variations must be included in models aimed at understanding at Lyα emission from LAEs and LBGs and similar objects.

Second, observed distribution functions of $EW(\mathrm{Ly}\alpha)_{obs}$ and the Lyα luminosity function must be strongly modified by radiation transfer and dust effects, and the fraction of objects with low $EW(\mathrm{Ly}\alpha)_{obs}$ ($L(\mathrm{Ly}\alpha)$) must be "artificially" overestimated (cf. Paper II). For a proper interpretation this must be taken into account; simple corrections may be applied using e.g. the proposed extinction estimate (Eq. (4)) or more sophisticated methods.

Third, the long/constant star formation rates and "old" ages (∼20−100 Myr) of LBGs derived from stellar population studies can be reconciled with the observed Lyα properties, when radiation transfer and dust are taken into account. In these circumstances Lyα should be independent of the stellar population age (measured since the onset of SF); its strength and line profile are mostly determined by the extinction and by N_{HI} (at least in the case of a homogeneous expanding shell). Possible trends of Lyα emission with age, such as indicated e.g. by Shapley et al. (2001, 2003); Ferrara & Ricotti (2006); Pentericci et al. (2007) but apparently found to be conflicting among each other, should then be fortuitous.

Finally, our scenario should explain the increase of the ratio of LAE/LBG and a higher percentage of LBGs with strong Lyα emission with redshift. These trends were suggested earlier (see e.g. Hu et al. 1998) and are now observed (Noll et al. 2004; Shimasaku et al. 2006; Nagao et al. 2007; Ouchi et al. 2007; Dow-Hygelund et al. 2007; Reddy et al. 2007). Indeed if extinction decreases with increasing z as expected e.g. from the observed metallicity decrease with redshift (cf. Tremonti et al. 2004; Erb et al. 2006; Ando et al. 2007; Liu et al. 2008), our radiation transfer models presented here predict stronger Lyα emission (see Eq. (4)), even if the intrinsic Lyα emission properties remain the same. Stronger intrinsic emission is additionally expected with decreasing metallicity, due to changes of the ionising/stellar properties. Both effects will thus lead to stronger Lyα emission and hence to an increase of the LAE/LBG ratio with redshift.

7. Summary and conclusion

Our 3D Lyα and UV continuum radiation transfer code (Verhamme et al. 2006) has been applied to fit the Lyα line profiles of 11 LBGs with Lyα emission in the FORS Deep Field with redshifts between 2.8 and 5 observed with medium spectral resolution ($R \approx 2000$) by Tapken et al. (2007). The observed line profiles show a variety of morphologies, including commonly observed redshifted asymmetric profiles, two double-peak profiles, and other more complicated line shapes.

We have adopted a simple model with a spherically expanding shell, which consists of neutral hydrogen and mixed-in dust, surrounding a central starburst emitting a UV continuum plus Lyα recombination line radiation from its associated H II region. With such a model, described by 4 "shell parameters" (the shell velocity $V_{\rm exp}$, its column density $N_{\rm HI}$, the Doppler parameter b, the dust optical depth $\tau_{\rm a}$) and 2 "spectral parameters" ($EW_{\rm int}$ and $FWHM_{\rm int}$ of the input Lyα line), we have been able to successfully reproduce all the observed line profiles (see Sect. 3). For the majority of the 11 LBGs analysed here the medium resolution spectra allowed us to constrain these parameters with relatively few degeneracies. In particular we found that Lyα line profile fitting alone allows us to determine the amount of dust extinction.

The parameters we have derived for our sample behave as follows (see Sect. 4):

- The expansion velocity is typically between $V_{\rm exp} \sim 150{-}200$ km s^{-1}. Higher velocities (300–400 km s^{-1}) may be found in two objects. In two out of 11 LBGs the neutral medium is most likely quasi-static ($V_{\rm exp} \sim 10{-}25$ km s^{-1}); their double-peaked line profiles are clearly distinct from the majority of the spectra. Our velocity determinations are also supported by measurements of interstellar lines in three cases.
- Except for one object, FDF4691 with a double-peaked Lyα profile with $FWHM \sim 840$ km s^{-1}, all Lyα line profiles can be reproduced with a relatively low value of the intrinsic Lyα line width ($FWHM^{\rm int} \sim 100$ km s^{-1}); radiation transfer effects broaden the line to the observed widths of typically $FWHM^{\rm obs} \sim 200{-}600$ km s^{-1}. We have proposed that the observed $FWHM$(Lyα) is related to the H I column density to the first order.
- The radial H I column density obtained from our Lyα line fits ranges from $N_{\rm HI} \sim 2 \times 10^{19}$ to 7×10^{20} cm^{-2}. Lower values may also apply in a few objects. We found possible indications of an anti-correlation between the observed Lyα equivalent width and $N_{\rm HI}$, and for a correlation between $FWHM$(Lyα) and $N_{\rm HI}$.
- Our Lyα profile fits yield values of $E(B-V) \sim 0.05{-}0.2$ for the gas extinction. These values are also broadly in agreement with the extinction derived from broad-band SED fits for our objects. We found indications for a dust-to-gas ratio higher than the Galactic value, and for a substantial scatter.
- The escape fraction of Lyα photons $f_{\rm e}$, which follows from our Lyα profile fits, was found to be determined primarily by the extinction. We propose a simple fit between $f_{\rm e}$ and $E(B-V)$ (Eq. (3)), which for $E(B-V) \lesssim 0.3$ is also in reasonable agreement with the Lyα escape fraction measured in nearby starbursts. Since Lyα photons are more strongly suppressed by dust than UV continuum photons, a measurement of $EW(\text{Ly}\alpha)_{\rm obs}$ can in principle yield $E(B-V)$ (see Eq. (4)), provided the intrinsic Lyα equivalent width is known (or assumed).
- Although the LBGs modeled here include objects with observed Lyα equivalent widths down to ~6 Å in the rest-frame (and $EW(\text{Ly}\alpha)_{\rm obs}$ up to 130–150 Å), 10/11 objects can clearly be fit with higher intrinsic Lyα equivalent widths ($EW(\text{Ly}\alpha)_{\rm int} \sim 50{-}100$ Å or larger), which are expected for stellar populations forming constantly over long periods ($\gtrsim$10–100 Myr). In three cases we found indications for younger populations. This result agrees with the one found in Paper II from the modeling of cB58 – an LBG with Lyα in absorption – and shows that radiation transfer effects and dust can lead to a great diversity of observed Lyα strengths (and profile shapes), even if the intrinsic stellar populations and emission line properties of LBGs may be fairly similar.
- After correction for radiation transfer and dust effects we obtain a better consistency between the use of the Lyα and UV continuum luminosity as SFR indicators.

Putting together the model results from this paper (LBG with Lyα in emission) and those from Paper II (modeling of an LBG with Lyα in absorption) we have been able to reproduce the main trends/correlations found in large samples of LBGs and LAEs (see Sect. 4.9). In particular we found that the absence of high $EW_{\rm obs}$-high SFR objects is due to radiation transfer effects and the presence of dust. We also show that the observed correlation of velocity shifts between IS lines and Lyα with Lyα strength (cf. Shapley et al. 2003) does not reflect systematic differences of the outflow velocities.

We have proposed that most LBGs and LAEs intrinsically have $EW(\text{Ly}\alpha)_{\rm int} \sim 60{-}80$ Å or larger, and that the main physical parameters responsible for the observed variety of Lyα strengths and profiles in LBGs are $N_{\rm HI}$ and the accompanying variation of the dust content. These quantities, in turn, are thought to scale mostly with galaxy mass. Such relatively high intrinsic equivalent widths are compatible with expectations for relatively long star formation episodes ($\gtrsim$10–100 Myr), compatible with typical ages and star formation histories derived for LBGs. Interestingly we also found indications of relatively low extinction ($E(B-V) \lesssim 0.1$) LBGs with Lyα in absorption in the sample of Shapley and collaborators. If true, these could be short duty-cycle, post-starburst objects, dominated by stellar Lyα absorption.

Analysing the properties of LBGs and LAEs at $z \sim 3$ we have shown that there is a clear overlap between these two populations (Sect. 6.1): ~20–25% of the LBGs of Shapley et al. (2003) – those with $EW(\text{Ly}\alpha)^{\rm rest}_{\rm obs} > 20$ Å – correspond to LAEs brighter than $R_{\rm AB} = 25.5$ mag. The remaining ~77% of the statistically complete LAE population from Gronwall et al. (2007) are fainter in the continuum than the LBGs. Radiation transfer, dust effects, and changes in the stellar/ionising properties should also explain the increase of the LAE/LBG ratio, and a higher percentage of LBGs with strong Lyα emission with increasing redshift.

Our Lyα line profile fitting of LBGs with a detailed radiation transfer code has shown that we are able to understand a diversity of Lyα line shapes and strengths and thereby to provide interesting quantitative constraints on their gas and stellar properties. Most of the observed differences and correlations between Lyα and other properties can be understood with a simple outflow model, where the H I column density and dust content ($E(B-V)$) play the main roles. The same model applies to LAEs, which appear to be closely related to LBGs.

Several additional tests of our scenario have been proposed and new questions have been raised, e.g. about the star formation duration of some LBGs with apparently low extinction (see Sect. 6.3). Numerous interesting implications remain to be

investigated, e.g. on the interpretation of Lyα luminosity functions. It is the hope that radiation transfer models, such as those successfully applied here, will help to shed further light on star formation and galaxy evolution at high redshift.

Acknowledgements. We thank Daniela Calzetti for unpublished measurements of $N_{\rm HI}$ in local starbursts, and Alice Shapley and Caryl Gronwall for communicating data in electronic form. We thank many colleagues for stimulating discussions during the last years and at the Lyα workshop held recently in Paris. Matthew Hayes, Andrea Ferrara, and David Valls-Gabaud, provided useful comments on an earlier version of the manuscript. This work was supported by the Swiss National Science Foundation.

References

Adelberger, K. L., Steidel, C. C., Shapley, A. E., & Pettini, M. 2003, ApJ, 584, 45
Adelberger, K. L., Steidel, C. C., Pettini, M., et al. 2005, ApJ, 619, 697
Ahn, S.-H., Lee, H.-W., & Lee, H. M. 2000, J. Korean Astron. Soc., 33, 29
Ahn, S.-H., Lee, H.-W., & Lee, H. M. 2002, ApJ, 567, 922
Ajiki, M., Taniguchi, Y., Fujita, S. S., et al. 2003, AJ, 126, 2091
Ando, M., Ohta, K., Iwata, I., et al. 2004, ApJ, 610, 635
Ando, M., Ohta, K., Iwata, I., et al. 2007, PASJ, 59, 717

Atek, H., Kunth, D., Hayes, M., & Ostlin, G. 2008, A&A, submitted
Baker, A. J., Tacconi, L. J., Genzel, R., Lehnert, M. D., & Lutz, D. 2004, ApJ, 604, 125
Bender, R., Appenzeller, I., Böhm, A., et al. 2001, in Deep Fields, ed. S. Cristiani, A. Renzini, & R. E. Williams, 96
Bohlin, R. C., Savage, B. D., & Drake, J. F. 1978, ApJ, 224, 132
Calzetti, D. 2001, PASP, 113, 1449
Calzetti, D., Armus, L., Bohlin, R. C., et al. 2000, ApJ, 533, 682
Cantalupo, S., Porciani, C., Lilly, S. J., & Miniati, F. 2005, ApJ, 628, 61
Christensen, L., Sánchez, S. F., Jahnke, K., et al. 2004, A&A, 417, 487
Cuby, J.-G., Hibon, P., Lidman, C., et al. 2007, A&A, 461, 911
Daddi, E., Dickinson, M., Morrison, G., et al. 2007, ApJ, 670, 156
Dawson, S., Rhoads, J. E., Malhotra, S., et al. 2004, ApJ, 617, 707
de Mello, D. F., Leitherer, C., & Heckman, T. M. 2000, ApJ, 530, 251
Delgado, R. M. G., Cerviño, M., Martins, L. P., Leitherer, C., & Hauschildt, P. H. 2005, MNRAS, 357, 945
Dijkstra, M., & Wyithe, J. S. B. 2007, MNRAS, 379, 1589
Dijkstra, M., Haiman, Z., & Spaans, M. 2006a, ApJ, 649, 14
Dijkstra, M., Haiman, Z., & Spaans, M. 2006b, ApJ, 649, 14
Dow-Hygelund, C. C., Holden, B. P., Bouwens, R. J., et al. 2007, ApJ, 660, 47
Elbaz, D., Daddi, E., Le Borgne, D., et al. 2007, A&A, 468, 33
Ellingson, E., Yee, H. K. C., Bechtold, J., & Elston, R. 1996, ApJ, 466, L71
Erb, D. K., Shapley, A. E., Steidel, C. C., et al. 2003, ApJ, 591, 101
Erb, D. K., Shapley, A. E., Pettini, M., et al. 2006, ApJ, 644, 813
Faucher-Giguere, C. ., Prochaska, J. X., Lidz, A., Hernquist, L., & Zaldarriaga, M. 2007, ArXiv e-prints, 709
Ferrara, A., & Ricotti, M. 2006, MNRAS, 373, 571
Finkelstein, S. L., Rhoads, J. E., Malhotra, S., Grogin, N., & Wang, J. 2007a, ArXiv e-prints, 708
Finkelstein, S. L., Rhoads, J. E., Malhotra, S., Pirzkal, N., & Wang, J. 2007b, ApJ, 660, 1023
Fosbury, R. A. E., Villar-Martín, M., Humphrey, A., et al. 2003, ApJ, 596, 797
Gabasch, A., Bender, R., Seitz, S., et al. 2004, A&A, 421, 41
Gawiser, E., van Dokkum, P. G., Gronwall, C., et al. 2006, ApJ, 642, L13
Gawiser, E., Francke, H., Lai, K., et al. 2007, ApJ, 671, 278
Grimes, J. P., Heckman, T., Strickland, D., et al. 2007, ApJ, 668, 891
Gronwall, C., Ciardullo, R., Hickey, T., et al. 2007, ApJ, 667, 79
Hansen, M., & Oh, S. P. 2006, MNRAS, 367, 979
Hayes, M., Östlin, G., Mas-Hesse, J. M., et al. 2005, A&A, 438, 71
Hayes, M., Östlin, G., Atek, H., et al. 2007, MNRAS, 382, 1465
Heckman, T. M., Sembach, K. R., Meurer, G. R., et al. 2001, ApJ, 558, 56
Heidt, J., Appenzeller, I., Gabasch, A., et al. 2003, Ap&SS, 284, 385
Hu, E. M., Cowie, L. L., & McMahon, R. G. 1998, ApJ, 502, L99
Kashikawa, N., Shimasaku, K., Malkan, M. A., et al. 2006, ApJ, 648, 7
Kennicutt, Jr., R. C. 1998, ARA&A, 36, 189
Kobayashi, M. A. R., Totani, T., & Nagashima, M. 2007, ApJ, 670, 919
Kovač, K., Somerville, R. S., Rhoads, J. E., Malhotra, S., & Wang, J. 2007, ApJ, 668, 15
Kudritzki, R.-P., Méndez, R. H., Feldmeier, J. J., et al. 2000, ApJ, 536, 19
Kunth, D., Mas-Hesse, J. M., Terlevich, E., et al. 1998, A&A, 334, 11
Lai, K., Huang, J.-S., Fazio, G., et al. 2007, ApJ, 655, 704
Lai, K., Huang, J.-S., Fazio, G., et al. 2008, ApJ, 674, 70
Laursen, P., Razoumov, A. O., & Sommer-Larsen, J. 2008, ArXiv e-prints, 805
Le Delliou, M., Lacey, C. G., Baugh, C. M., & Morris, S. L. 2006, MNRAS, 365, 712
Lequeux, J., Kunth, D., Mas-Hesse, J. M., & Sargent, W. L. W. 1995, A&A, 301, 18
Liu, X., Shapley, A. E., Coil, A. L., Brinchmann, J., & Ma, C.-P. 2008, ArXiv e-prints, 801
Malhotra, S., & Rhoads, J. E. 2002, ApJ, 565, L71
Mao, J., Lapi, A., Granato, G. L., de Zotti, G., & Danese, L. 2007, ApJ, 667, 655
Martin, C., Sawicki, M., Dressler, A., & McCarthy, P. 2008, ApJ, submitted
Mas-Hesse, J. M., Kunth, D., Tenorio-Tagle, G., et al. 2003, ApJ, 598, 858
Mehlert, D., Tapken, C., Appenzeller, I., et al. 2006, A&A, 455, 835
Misawa, T., Tytler, D., Iye, M., et al. 2007, AJ, 134, 1634
Mori, M., & Umemura, M. 2006, Nature, 440, 644
Nagamine, K., Ouchi, M., Springel, V., & Hernquist, L. 2008, ArXiv e-prints, 802
Nagao, T., Murayama, T., Maiolino, R., et al. 2007, A&A, 468, 877
Neufeld, D. A. 1990, ApJ, 350, 216
Neufeld, D. A. 1991, ApJ, 370, L85
Nilsson, K. K., Møller, P., Möller, O., et al. 2007, A&A, 471, 71
Noeske, K. G., Weiner, B. J., Faber, S. M., et al. 2007, ApJ, 660, L43
Noll, S., Mehlert, D., Appenzeller, I., et al. 2004, A&A, 418, 885
Ouchi, M., Shimasaku, K., Akiyama, M., et al. 2007, ArXiv e-prints, 707
Overzier, R. A., Bouwens, R. J., Cross, N. J. G., et al. 2008, ApJ, 673, 143
Papovich, C., Dickinson, M., & Ferguson, H. C. 2001, ApJ, 559, 620
Pentericci, L., Grazian, A., Fontana, A., et al. 2007, A&A, 471, 433
Pettini, M., Steidel, C. C., Adelberger, K. L., Dickinson, M., & Giavalisco, M. 2000, ApJ, 528, 96
Pettini, M., Rix, S. A., Steidel, C. C., et al. 2002, ApJ, 569, 742
Pierleoni, M., Maselli, A., & Ciardi, B. 2007, ArXiv e-prints, 712
Pirzkal, N., Xu, C., Ferreras, I., et al. 2006, ApJ, 636, 582
Pirzkal, N., Malhotra, S., Rhoads, J. E., & Xu, C. 2007, ApJ, 667, 49
Rauch, M., Haehnelt, M., Bunker, A., et al. 2007, ArXiv e-prints, 711
Reddy, N. A., Steidel, C. C., Fadda, D., et al. 2006, ApJ, 644, 792
Reddy, N. A., Steidel, C. C., Pettini, M., et al. 2007, ArXiv e-prints, 706
Rhoads, J. E., Dey, A., Malhotra, S., et al. 2003, AJ, 125, 1006
Richling, S., Meinköhn, E., Kryzhevoi, N., & Kanschat, G. 2001, A&A, 380, 776
Savaglio, S., Panagia, N., & Padovani, P. 2002, ApJ, 567, 702
Schaerer, D. 2003, A&A, 397, 527
Schaerer, D. 2007, ArXiv e-prints, 706
Schaerer, D., & Pelló, R. 2005, MNRAS, 362, 1054
Schaerer, D., & Verhamme, A. 2008, A&A, 480, 369
Seaton, M. J. 1979, MNRAS, 187, 73P
Shapley, A. E., Steidel, C. C., Adelberger, K. L., et al. 2001, ApJ, 562, 95
Shapley, A. E., Steidel, C. C., Pettini, M., & Adelberger, K. L. 2003, ApJ, 588, 65
Shimasaku, K., Kashikawa, N., Doi, M., et al. 2006, PASJ, 58, 313
Stark, D. P., Ellis, R. S., Richard, J., et al. 2007a, ApJ, 663, 10
Stark, D. P., Loeb, A., & Ellis, R. S. 2007b, ApJ, 668, 627
Taniguchi, Y., Ajiki, M., Nagao, T., et al. 2005, PASJ, 57, 165
Tapken, C. 2005, Ph.D. Thesis, Landessternwarte Heidelberg
Tapken, C., Appenzeller, I., Mehlert, D., Noll, S., & Richling, S. 2004, A&A, 416, L1
Tapken, C., Appenzeller, I., Gabasch, A., et al. 2006, A&A, 455, 145
Tapken, C., Appenzeller, I., Noll, S., et al. 2007, A&A, 467, 63
Tasitsiomi, A. 2006, ApJ, 645, 792
Teplitz, H. I., McLean, I. S., Becklin, E. E., et al. 2000, ApJ, 533, L65
Thommes, E., & Meisenheimer, K. 2005, A&A, 430, 877
Thuan, T. X., & Izotov, Y. I. 1997, ApJ, 489, 623
Tremonti, C. A., Heckman, T. M., Kauffmann, G., et al. 2004, ApJ, 613, 898
Vanzella, E., Cristiani, S., Dickinson, M., et al. 2008, A&A, 478, 83
Venemans, B. P., Röttgering, H. J. A., Overzier, R. A., et al. 2004, A&A, 424, L17
Venemans, B. P., Röttgering, H. J. A., Miley, G. K., et al. 2005, A&A, 431, 793
Verhamme, A., Schaerer, D., & Maselli, A. 2006, A&A, 460, 397
Vladilo, G., Prochaska, J. X., & Wolfe, A. M. 2007, ArXiv e-prints, 712
Willis, J. P., & Courbin, F. 2005, MNRAS, 357, 1348
Wilman, R. J., Gerssen, J., Bower, R. G., et al. 2005, Nature, 436, 227
Yamada, S. F., Sasaki, S. S., Sumiya, R., et al. 2005, PASJ, 57, 881